Summer 2019

Passive harmonic generation at spring contacts

Sen Yang

PASSIVE HARMONIC GENERATION AT SPRING CONTACTS

by

SEN YANG

A DISSERTATION

Presented to the Faculty of the Graduate School of the

MISSOURI UNIVERSITY OF SCIENCE AND TECHNOLOGY

In Partial Fulfillment of the Requirements for the Degree

DOCTOR OF PHILOSOPHY

in

ELECTRICAL ENGINEERING

2019

Approved by:

David Pommerenke, Advisor
Jun Fan
Victor Khilkevich
Chulsoon Hwang
Daniel Fischer

PUBLICATION DISSERTATION OPTION

This dissertation consists of the following three articles, formatted in the style used by the Missouri University of Science and Technology:

Paper I: Pages 3-30 are intended for submission to IEEE Transactions on Electromagnetic Compatibility.

Paper II: Pages 31-57 have been published on IEEE Transactions on Instrumentation and Measurement.

Paper III: Pages 58-81 have been published on IEEE Transactions on Electromagnetic Compatibility.

ABSTRACT

In the first paper, the RF passive harmonic generation phenomenon on the spring contact is studied. A spring contact harmonic generation measurement system is developed. The factors that may have an impact on the spring contact harmonic generation, such as contact material, contact force, and contact resistance are characterized by the measurement system. The gold-to-gold contact is found to be much superior to the stainless-steel contacts. It is also found that the passive nonlinearity at the spring contact is the semiconductor-like junction formed by the surface oxide film.

In the second paper, we show that the maximum E-field coupling occurs at a location slightly offset from the trace center. The E-field coupling to a shielded H-field probe at such a position leads to differential mode coupling which the standard shield of an H-field probe is unable to suppress. The coupling mechanism is investigated and a differential E-field coupling suppression approach is proposed.

In the third paper, a measurement system which uses acoustic vibration to locate passive intermodulation (PIM) sources in base station antennas is presented. This measurement system uses mechanical vibration to modulate the PIM signal. By introducing the acoustic vibration at different locations in the base station antenna and observing if the PIM signal is modulated by the acoustic frequency, the most likely location of the PIM source is identified.

ACKNOWLEDGMENTS

TABLE OF CONTENTS

SECTION

LIST OF ILLUSTRATIONS

PAPER II

PAPER III

LIST OF TABLES

1. INTRODUCTION

Spring contacts are used in mobile devices to ground the metal planes near the antennas. Inappropriate design of the spring contact will cause harmonic generation at the contact which will deteriorate the receiver sensitivity of the mobile system.

In the first paper, the RF passive harmonic generation phenomenon on the spring contact is studied. A spring contact harmonic generation measurement system is developed. The factors that may have an impact on the spring contact harmonic generation, such as contact material, contact force, and contact resistance are characterized by the measurement system. The gold-to-gold contact is found to be much superior to the stainless-steel contacts. It is also found that the passive nonlinearity at the spring contact is the semiconductor-like junction formed by the surface oxide film.

In the second paper, we show that the maximum E-field coupling occurs at a location slightly offset from the trace center. The E-field coupling to a shielded H-field probe at such a position leads to differential mode coupling which the standard shield of an H-field probe is unable to suppress. The coupling mechanism is investigated and a differential E-field coupling suppression approach is proposed. For the H-field probe used in this work, a proposed floating plate is shown to improve the measured E-field suppression ratio by a factor of 18 dB compared to a similar probe without this modification.

In the third paper, a measurement system which uses acoustic vibration to locate passive intermodulation (PIM) sources in base station antennas is presented. This measurement system uses mechanical vibration to modulate the PIM signal. The

modulation of the PIM signal is detected, and its strength or presence/absence is used as guidance for selecting the location of the vibrating transducer. For the method to be successful, the PIM signal must be caused by loose mechanical contacts or loose nonlinear materials. By introducing the acoustic vibration at different locations in the base station antenna and observing if the PIM signal is modulated by the acoustic frequency, the most likely location of the PIM source is identified.

The primary contributions of this dissertation include:

Paper I: 1) A fully automated measurement setup for spring contact harmonic generation. 2) Investigation of the harmonic generation mechanism at the spring contact. It is found that the semiconductor-like junction is the main source of harmonics. 3) Experimentally characterization of the spring contact harmonic generation.

Paper II: 1) Discovered the differential E-field coupling to the shielded H-field probe. 2). Proposed the floating plate method to suppress the differential E-field coupling.

Paper III: 1) Proposed the methodology of vibration modulation to detect PIM source. 2) Designed and manufactured the ultrasonic vibration system and RF demodulation system utilizing the vibration modulation method.

Other contributions during the Ph.D. candidate period include: Near-field scan area [1]-[3]; ElectroStatic Discharge (ESD) area [4]-[10]; Passive nonlinearity area [11]-[16]; and Electromagnetic Compatibility area [17].

PAPER

I. EXPERIMENTAL CHARACTERIZATION OF THE HARMONIC GENERATION AT THE SPRING CONTACT IN A MOBILE DEVICE

ABSTRACT

Spring contacts are used in mobile devices to ground the metal planes near the antennas. Inappropriate design of the spring contact will cause harmonic generation at the contact which will deteriorate the receiver sensitivity of the mobile system. In this paper, the RF passive harmonic generation phenomenon on the spring contact is studied. A spring contact harmonic generation measurement system is developed. The factors that may have an impact on the spring contact harmonic generation, such as contact material, contact force, and contact resistance are characterized by the measurement system. The gold-to-gold contact is found to be much superior to the stainless-steel contacts. It is also found that the passive nonlinearity at the spring contact is the semiconductor-like junction formed by the surface oxide film. Recommendations to reduce the harmonic generation at the spring contacts are discussed in the last section of the paper.

1. INTRODUCTION

Mobile devices nowadays are equipped with various radio technologies such as 4G/5G cellular technologies, Wi-Fi, Bluetooth, Global Positioning System (GPS), Near Field Communication (NFC), etc. Many of these radio technologies feature very low

receiver (RX) power, which results in being very sensitive to the in-band interference. Although different radio technologies often operate in the different frequency band and seem to be unlikely to interfere with each other, considering the compact size of the mobile devices, there are several mechanisms that cause inter-technology interference. The multi-radio signal coexistence (COEX) has become a growing concern for the industry. Improper handling of the COEX issues will lead to failure in the receiver sensitivity test. The harmonics generated at the spring contacts near the antennas are one of the main contributors to the COEX issues in the mobile devices. For example, an 800 MHz cellular transmitting (TX) signal at the spring contact may generate a third order harmonic of 2400 MHz, which falls into the Wi-Fi band, will couple back to the Wi-Fi receiver and thus greatly reduce the Wi-Fi receiver sensitivity.

Multiple metal planes exist in a mobile device, such as display panel, printed circuit board (PCB), back panel, etc. The antennas are often close to these metal planes due to the compact size of the mobile system. If left ungrounded, these metal planes will shift antennas' operating frequencies and reduce the antenna performance. Spring contacts are used to ground the metal planes near the antennas. The use of the springs increases flexibility during the manufacturing and the repair process. The springs are often placed close to the antennas to achieve the best grounding effort. Strong TX signal flows through the spring contacts and induces the harmonics which will couple back to the victim RX system. The systematical characterization of the spring contact harmonic generation phenomenon is necessary for the designers to reduce the harmonic interference and to achieve the best cost-effectiveness.

The harmonic generation of the electrical contacts has been a subject of research for decades [1]-[5]. The total harmonic distortion is used as an indicator of relay switch contact health [1][3]. However, these electrical contact harmonic study only focused on audio frequency distortion, i.e. 10 kHz base frequency and the third harmonic of 30 kHz. The harmonic generation of electrical contact in the radio frequency (RF) band is not well studied. When subjected to high RF power, the passive component may demonstrate weak nonlinearity for various reasons, such as Metal-Insulator-Metal (MIM) junctions, ferromagnetic material, electro-thermal effect, etc. Passive intermodulation (PIM) is one of the passive nonlinearities that have been well-known and well-studied [6]-[20], which is often seen in the satellite communication and cellular base station industries. There is a distinct difference between the PIM and harmonic generation: 1) The PIM problem involves at least two base RF tones and the intermodulation product is of the concern while the harmonic generation only involves in one base RF tones. 2) The PIM problem involves much higher TX power than the harmonic generation. The PIM test standard [12] requires two 43dBm (20 W) base tones while the harmonic generation in the mobile devices only requires 23 dBm (200 mW). 3) The test setup of the PIM is different from the harmonic generation. The test equipment for PIM is the PIM tester, which consists of two RF signal source, power amplifiers (PA), and duplexers. On the other hand, there is no existing test equipment for the spring contact harmonic measurement.

Thus, it is necessary to characterize the harmonic generation at the spring contact at the RF band. In Section II, a measurement system for the spring contact harmonic generation is proposed. In Section III, the possible mechanism of the spring contact harmonic generation is explored and the potential contributors to the spring contact

harmonic generation are characterized by the proposed measurement system. In Section IV, discussion and recommendations are given for reducing the spring contact harmonic generation.

2. MEASUREMENT SYSTEM FOR SPRING CONTACT HARMONIC GENERATION

The harmonic generation measurement system is designed to measure the harmonics generated at the spring contact under certain conditions. The parameters that may contribute to the harmonic generation are investigated. As shown in the system block diagram in Figure 1, the measurement system consists of An Agilent RF signal generator N5181A, a power amplifier (PA) Minicircuits ZHL-4240W, a directional coupler, diplexer, the spring contact test vehicle, a force gauge with the serial port output, a xyz-stage system with step motors, a power divider Minicircuits ZN2PD2-50-S+, and an spectrum analyzer (SA) Agilent N4448A. To investigate the repeatability of the contacts and to achieve statistical conclusion, a large number of repetitive contact tests have to be performed. The signal generator, the xyz stage, the force gauge, and the spectrum analyzer are controlled by a laptop via Python scripts.

2.1. SPRING CLIPS IN THE MOBILE DEVICE

The spring clips in mobile devices are usually made of stainless steel (SUS). The contact point of the spring is usually gold-plated to achieve best contact effect. However, due to the cost-effectiveness concern, the gold-plated tip is undesirable for its high cost. The stainless-steel contacts, SUS-SUS, are better options in terms of cost. However, it is

found that SUS-SUS contact generates much higher harmonics than the gold contacts.
The spring used in this paper is designed for a nominal contact force of 0.4 N.
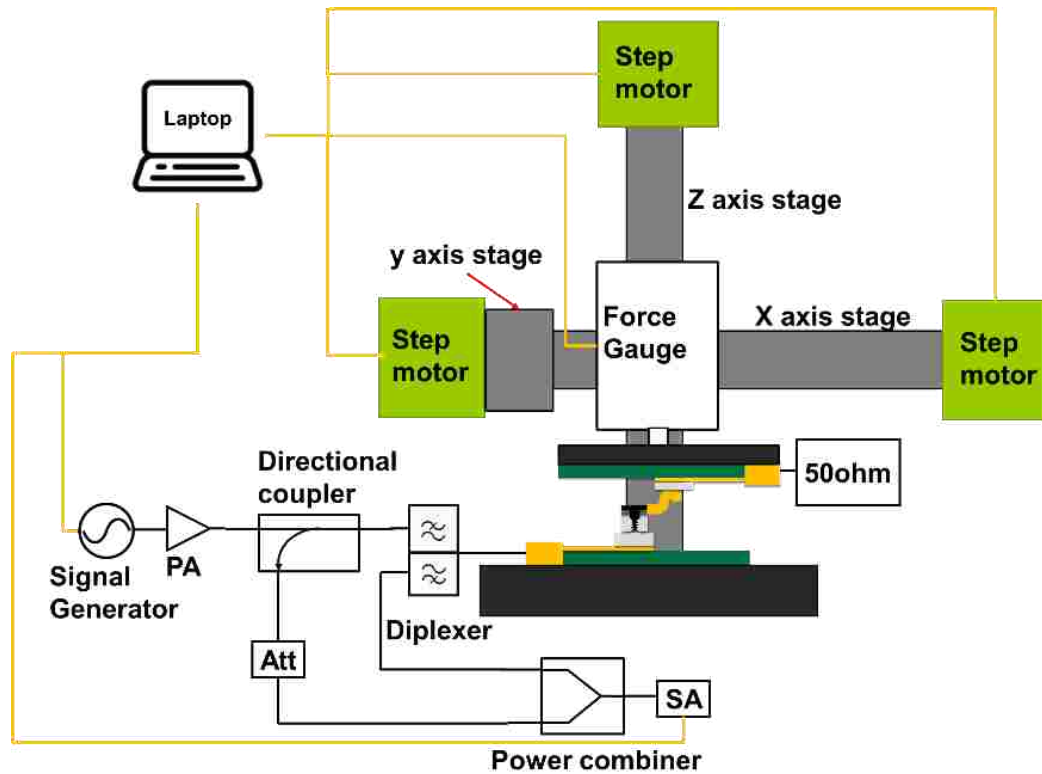
Figure 1. Spring contact harmonic measurement system block diagram.

Two types of springs are investigated in this work: 1) the springs with the gold-plated tip and 2) the springs without the gold-plated tip. They will be referred to as gold spring and SUS spring in the later section for simplicity. The spring tip touches the landing pads. The landing pads are also made from stainless steel. The gold-plated landing pad and the stainless-steel landing pad will be tested in this study. They will be referred to as gold pad and SUS pad in the later sections. The spring clip and the landing pad which are mounted on the test vehicle is shown in Figure 2.

2.2. SPRING CONTACT TEST VEHICLE

The spring contact test vehicle consists of a top microstrip line board and a bottom microstrip line board (Figure 3). The top microstrip line board hosts the landing pad while the bottom microstrip line board hosts the spring. The two boards are fixed by the 3D printed holders. The top board is attached to the force gauge, which is then attached to the xyz-stage.

The nominal contact force for the spring clip is 0.4N. The contact force has to be well controlled at this level in the experiment. The force gauge has a measuring range of 0 to 10 N force with the accuracy of 0.01 N, the instant force data can be read by the laptop via the serial port. The xyz-stage is controlled by the step motors. The step size of the xyz-stage movement is 1/3200 mm. The xyz-stage is also controlled by the laptop via its special communication protocol. The z-direction stage controls the movement of making contact and detaching. The x and y-direction stages control the spring to make contact at new locations on the pad so that the surface of both the spring tip and the landing pad will not be damaged over repetitive contacts at the same location.

2.3. TX BASE FREQUENCY SIGNAL PATH

The goal of the TX signal path is to deliver only the base frequency TX signal to the DUT while eliminating other frequency components (Figure 4). The base frequency signal is generated by the signal generator and then amplified by the power amplifier. The power amplifier has a fixed gain of 40 dB and P1dB of 2W, up to 4 GHz. The input TX power at the DUT is controlled by the signal generator's output power. The frequency components after the power amplifier will unavoidably contain harmonics of

the base frequency. The diplexer is essentially a low pass filter for the TX signal path and a high pass filter for the harmonic signal path. The harmonic components of the TX base frequency signal are removed by the low pass filter in the diplexer. The typical TX power at the DUT input port is 23 dBm (200 mW).
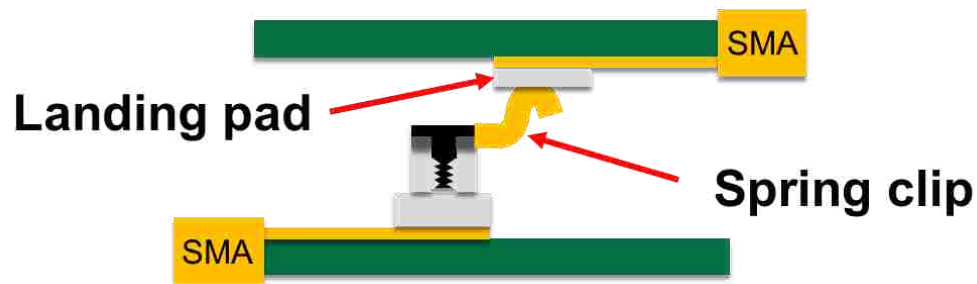
Figure 2. Spring clip and landing pad.

2.4. RX HARMONIC FREQUENCY SIGNAL PATH

The harmonics generated at the spring contact at the test vehicle will propagate back to the input port and then pass through the high pass filter port of the diplexer (Figure 4). The diplexer is the core component of the setup. High isolation between the TX band and the RX harmonic band are highly desired because excessive TX power coupled to the RX harmonic band will generate harmonics in the SA itself. The experience with the SA is that -60 dBm TX frequency signal at the SA will generate the third harmonic that is smaller than -120 dBm by the SA itself. The customized diplexer used in this measurement setup has the excellent TX to RX band isolation of over 100 dB.

2.5. CONTACT DETECTION

Considering the small contact area of the spring contacts and the bulk size of the hosting PCBs, it is difficult to visually check if the spring is making good contact with the landing pad. Thus, a contact detection path is designed into the measurement system (Figure 4). The reflected TX signal is used as an indicator of contact. The directional coupler couples a small amount of reflected TX signal and is measured by the SA. The reflected TX signal is high when the spring does not contact with the landing pad because the DUT is in the open state. When the spring makes contact with the landing pad, the reflected TX signal is reduced because the DUT is terminated by a 50 Ω load at the other side. By detecting the reduction of the reflected TX signal power, it can determine if the spring is making solid contact with the landing pad. The attenuator is needed here to reduce the coupled TX base frequency signal power so that it won't induce harmonics in the SA.
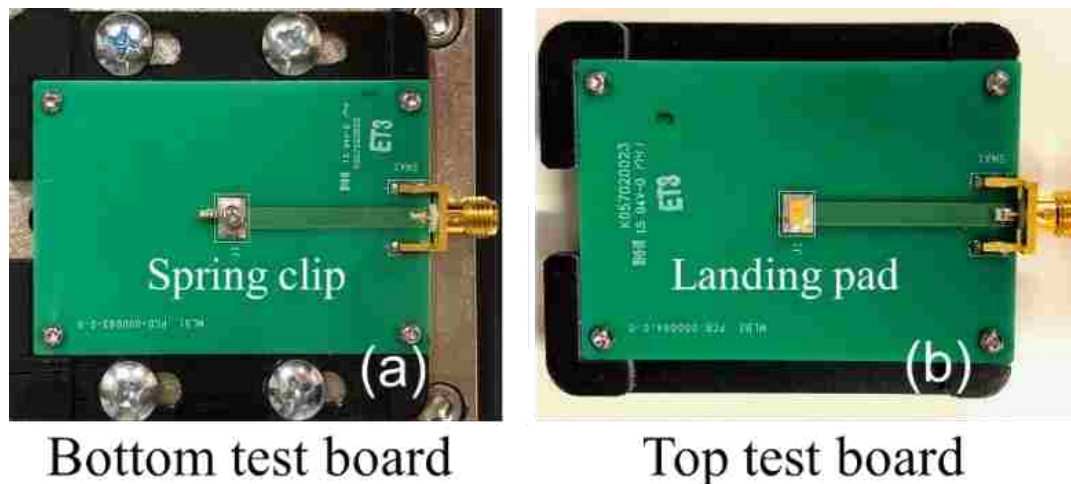
Figure 3. Spring contact test vehicle boards.

2.6. AUTOMATED MEASUREMENT

As mentioned previously, many contact tests have to be done for the spring

contact harmonic generation study. A measurement automation setup is developed for

this purpose. The Python scripts are developed to control the instruments used in the

measurement setup. The PyVisa module [21] is used to communicate with the signal

generator, spectrum analyzer, and the force gauge. The control code for the xyz-stage

step motors is developed based on the step motor driver's dynamic link library (DLL).

The control codes for each instrument are integrated to perform the specific harmonic

measurement task. For each round of contact-making, the movement and measurement

process are shown in the flow chart in Figure 5.
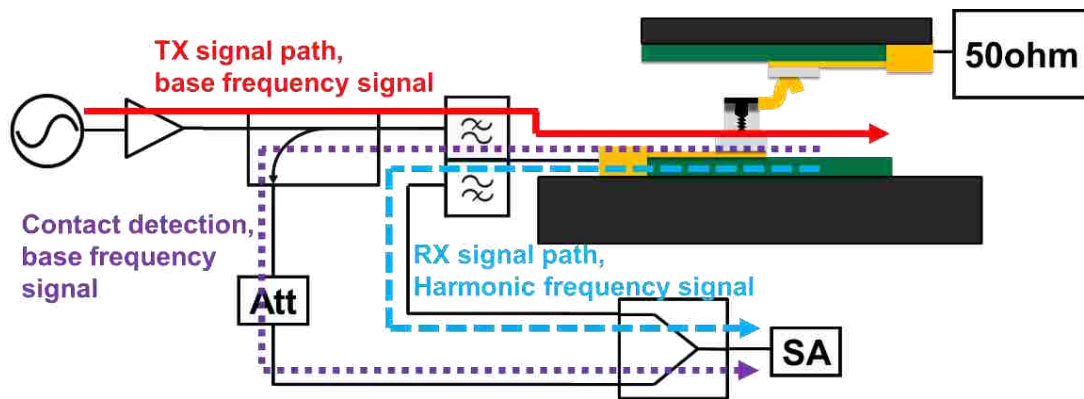
Figure 4. RF paths of the harmonic measurement system.

The harmonic measurement system in this work only measures the

reflected/backward harmonics. The forward harmonics are assumed to be equal to the

backward ones. This is because the spring contact can be seen as a point source in the

middle of a transmission line system. To verify this assumption, the backward and

forward harmonics were measured at the same time by the setup in Figure 6. The RF

relay controls the signal path that goes into the SA. The results in Figure 7 indicates that the forward and backward harmonics are at the same level as expected.
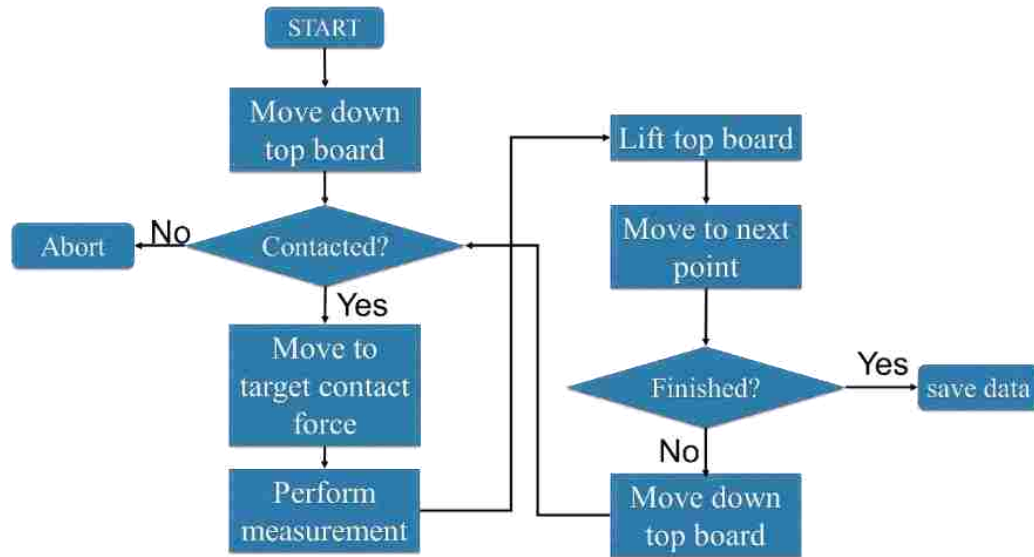
Figure 5. Flow chart of the automated measurement process.

3. SPRING CONTACT HARMONIC GENERATION MECHANISM

From the knowledge of the PIM generation, there are generally three types of passive nonlinearity sources: 1) The semiconductor-like junction. The surface oxide film on the contact surface acts as the Metal-Insulator-Metal junction, which has the semiconducting effect due to the tunnel effect. The MIM PIM generation has been studied extensively in previous works [17]-[20]. 2) The electro-thermal effect. The periodically heating caused by electrical signal will result in the periodically varying resistivity, which in turn inter-modulates with the carrier RF signal and generates PIM product. This is often found in the transmission line or lumped resistive component. 3)

Ferromagnetic effect. When the ferromagnetic material is subject to high RF power, it

will produce inter-modulated product of the carrier tones due to the ferromagnetic effect.
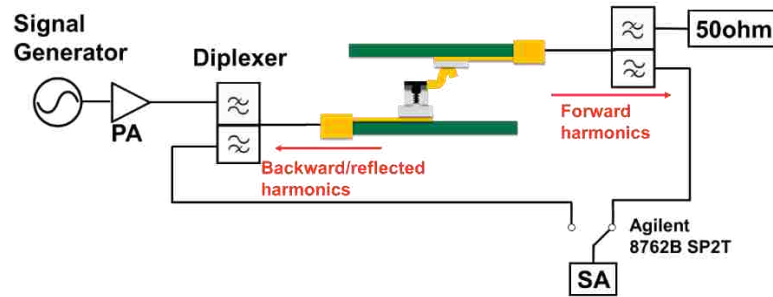
Figure 6. Measurement setup for forward and backward harmonic measurement.
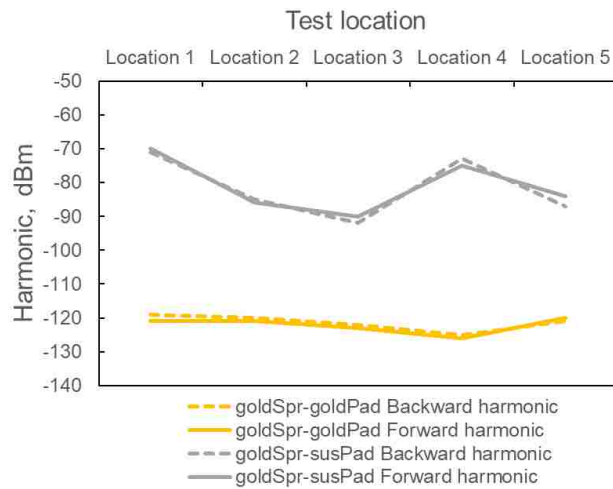
Figure 7. Measurement results of the forward and the backward harmonics.

3.1. REGROWTH RATE AS AN INDICATOR OF THE POTENTIAL HARMONIC SOURCES

As for the spring contact, since there is no ferromagnetic material involved, the

ferromagnetic effect should be ruled out first. On the other hand, it is difficult to directly

determine the mechanism by looking into the physics of the contact, due to the difficulty

of the test equipment. It is possible to look into other indicators. In [13], Henrie et al

reported that the electro-thermal induced nonlinearity behaves differently to the

semiconductor-like junction induced nonlinearity in terms of the regrowth rate. The

regrowth rate is essentially the slope of the input power versus the nonlinearity product

curve. For example, ideally, for a third order harmonic, 1 dB increase in the input power

will result in a 3 dB increase in the harmonic level, which has a regrowth rate of 3 dB/dB.

However, according to [13], when the input power grows sufficiently high, the regrowth

rate of semiconductor effect harmonic will decrease while on the contrary, the regrowth

rate of the electro-thermal effect induced harmonic will continue to increase to higher

than 3 dB/dB, as illustrated in Figure 8. The harmonic of stainless-steel spring and

stainless-steel landing pad (susSpr-susPad) was measured. The input power was swept

from 15 dBm to 23 dBm. The base frequency was 790 MHz and the 3rd harmonic

frequency was 2370MHz. As shown in Figure 9(b), the regrowth rate shows an obvious

decreasing trend with increasing input power. This is a clear indicator that the

semiconductor-like junction at the contact surface is the main nonlinearity mechanism at

the spring contact.

3.2. SPRING CONTACT HARMONIC GENERATION WITH DC BIAS

The regrowth rate has indicated that the harmonic source at the spring contact is

the semiconductor-like junction. To further investigate the semiconducting property of

the spring contact junction, the DC bias experiment was performed. Since the contact

resistance was unknown, it was better to have the DC current bias than the voltage bias.

The DC current bias measurement setup is shown in Figure 10. Two Keithley SMU

source meters were used in this setup. One SMU was used as the DC current source and the other was used as the voltage meter, which measured the voltage drop across the contact junction. The voltage meter was connected to the contact junction via 0603 12 kΩ resistors (Figure 11). To avoid potential junction melt-down when applying high DC current, the current was swept in a frog-leap scheme (Figure 12). The sweep started at 0 A bias and then increased one step to the positive and then jumped to the negative. At each current bias value, the second and third harmonics were measured.
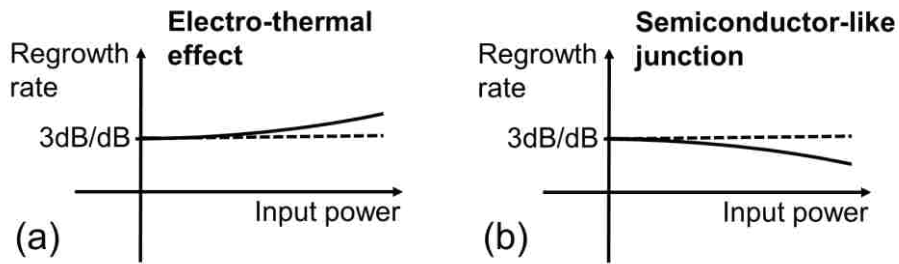
Figure 8. Opposite regrowth rate behavior.
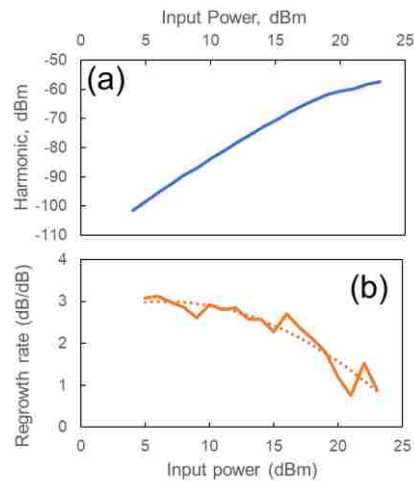
Figure 9. Plot of regrowth rate.
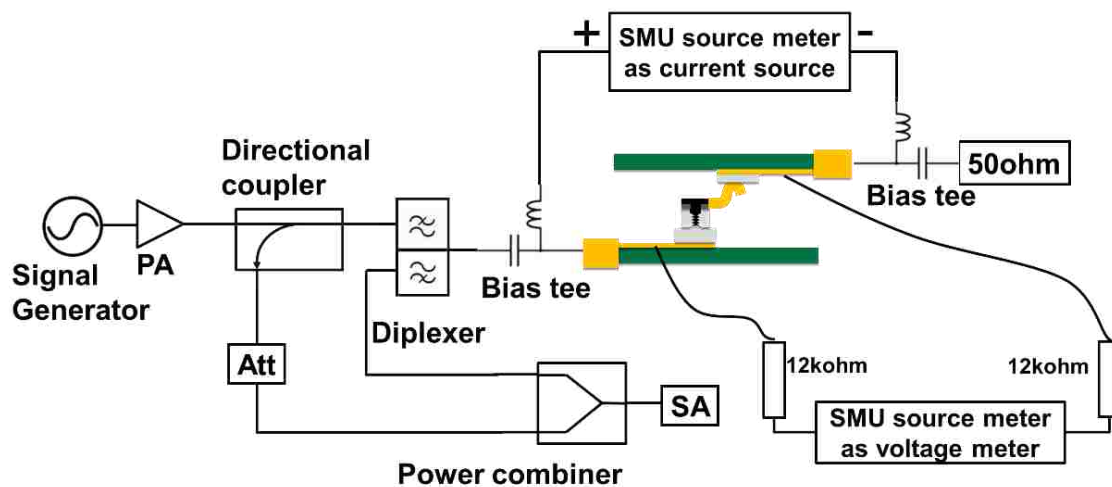
Figure 10. Measurement setup for spring contact harmonic generation with DC bias.
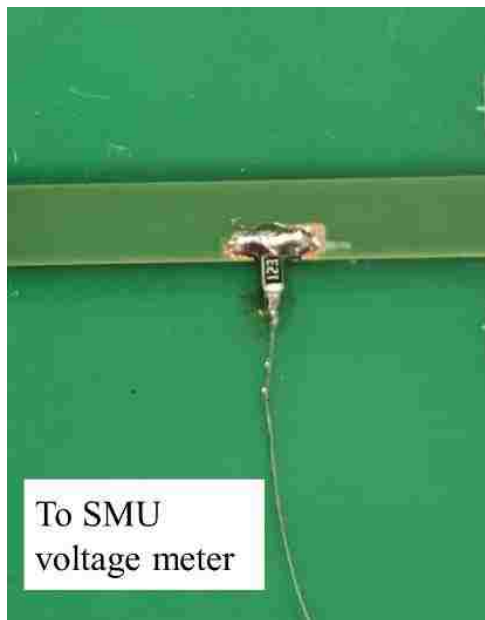
Figure 11. The 12 kΩ 0603 resistor.

The DC bias measurement was taken at the highest harmonic location, which had the third harmonic of -65 dBm. The measurement results of 2nd and 3rd harmonics are shown in Figure 13 and Figure 14. The second harmonic of the spring contact has a

notch at 0 A bias, then rises sharply to a high value and then drops down to low harmonic value again. The DC bias has enhanced the asymmetry of the junction and thus the second harmonic increased. The 3rd harmonic, however, remains high value for small current bias and then drops sharply to lower harmonic value. There is a voltage drop at $|I_{DC}|=0.07A$ in the voltage vs DC current bias plot (Figure 15) which indicates a drop in the contact resistance, the melting process of the contact junction starts at this point and thus reduced the harmonic level. The different behavior of 2nd and 3rd harmonic within 0.07A should attribute to the property of semiconductor-like junction itself.
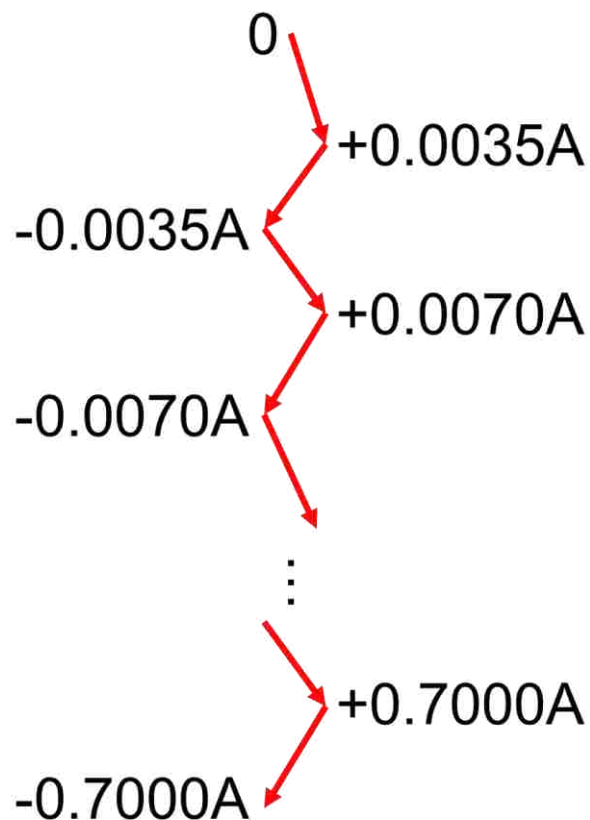
Figure 12. The fog-leap scheme of the DC current sweep.

The contact resistance was calculated from the current and voltage data (Figure 16). The resistance at 0 A was not symmetric, this is either because of the inaccuracy of the voltage measurement at a very small value, or some unknown asymmetry of the semiconducting contact junction.
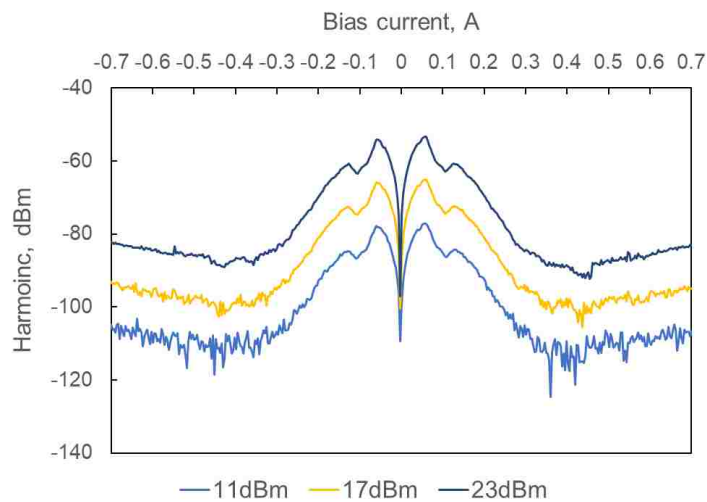
Figure 13. Second harmonic measurement results with DC bias.
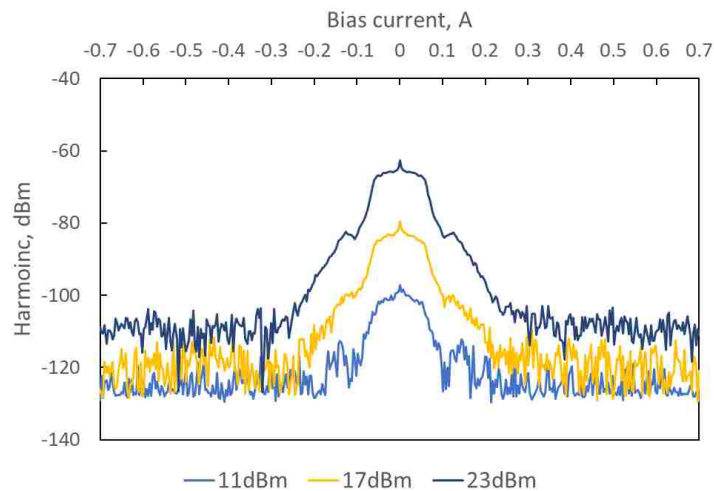
Figure 14. Third harmonic measurement results with DC bias.
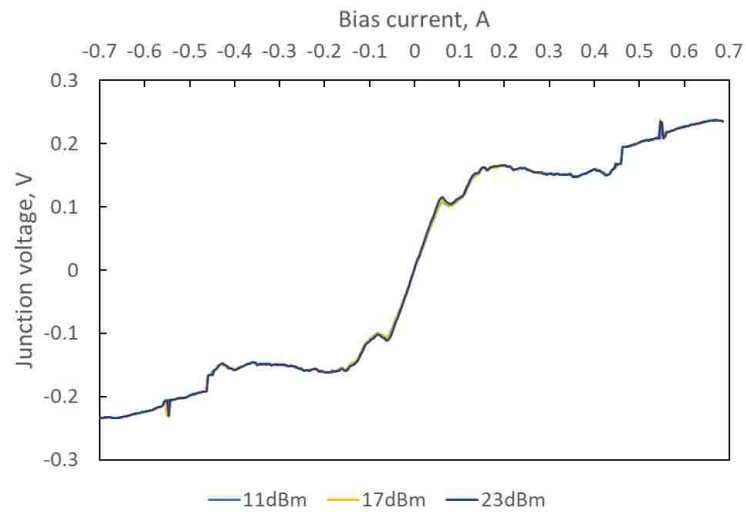
Figure 15. Contact junction voltage.
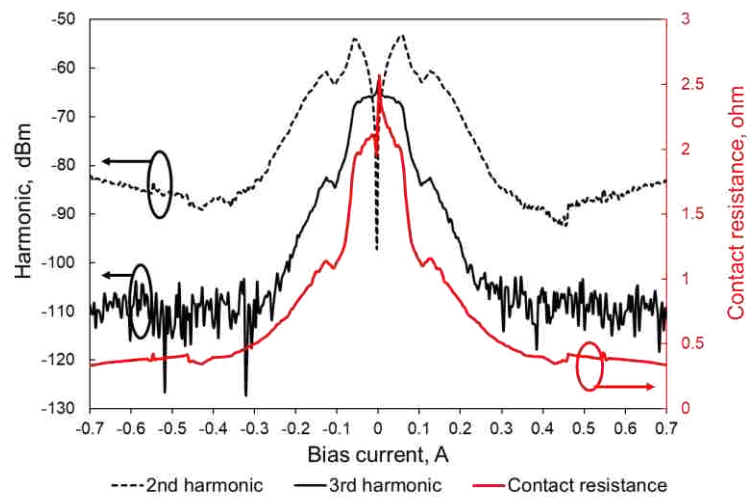
Figure 16. Contact resistance calculated from current and voltage data.

3.3. POSSIBLE HARMONIC GENERATION MECHANISM

The previous electrical contact harmonic generation works also indicate that the MIM junction is the main source of nonlinearity [1]-[5]. In [4], the MIM harmonic model is developed based on the tunnel effect. The MIM harmonic model is described by:

$$J^* = J_0 \phi_0 [\left(\frac{k}{2} - 1\right) v_0 + \frac{3}{128} \left(\frac{k^3}{6} - \frac{k^2}{2} - k\right) v_0^3 \sin t$$

$$- \frac{1}{128} \left(\frac{k^3}{6} - \frac{k^2}{2} - k\right) v_0^3 \sin 3t] \exp(-k) \tag{1}$$

where ϕ_0 is the work function of the contact metal, J_0 and k are the constant determined by thin film properties such as film thickness.

The MIM theory alone may not be able to explain the harmonic with the DC bias at the spring contact junction. Other semiconductor-like junction may exist at the same time. In the material research area, the semiconducting property of the sus surface oxide film has been reported by several research groups [22]-[27].

The oxide film itself demonstrates p-n junction property. Thus, the harmonics observed in the stainless-steel contact may originate from the p-n junction of the surface oxide. The formation of p-type and n-type dual layer oxide film [26] on the stainless-steel surface is shown in Figure 17. It is possible that the p-n junction of the stainless-steel surface oxide film has also contributed to the passive nonlinearity phenomenon that was observed in the DC bias experiment.

4. CHARACTERIZATION OF THE SPRING CONTACT HARMONIC GENERATION

4.1. CONTACT MATERIAL

This paper mainly investigates the gold-plated contact, stainless steel contact, and their combination. The gold-plated spring to gold plated landing pad (goldSpr-goldPad), gold-plated spring to stainless-steel landing pad (goldSpr-susPad), and stainless-steel

spring to stainless-steel landing pad (susSpr-susPad) were investigated. The contact force was 0.4 N. Eleven contact locations on the landing pad were tested with 0.2 mm distance. At each contact location, ten harmonic levels were recorded for every 10 seconds. In this way, the harmonic variation of the contact in both space and time were captured. The results are summarized in Figure 18. The solid line indicates the average harmonic level, while the error bars indicate the maximum and minimum harmonic value at each contact location. The goldSpr-goldPad contact showed the lowest harmonic level and the lowest variations, while the susSpr-susPad shows the highest harmonic level and the highest variations. The goldSpr-susPad contact scenario falls in between.

The spring contact harmonic generation mechanism is mainly the semiconductor-like junction formed by the surface oxide film. Gold as a member of noble metal has very stable chemical property, there is no surface oxide on the gold. Thus, there is no surface oxide film in the goldSpr-goldPad contact while in the susSpr-susPad contact, the surface oxide film exists on both sides of the contact. As for goldSpr-susPad scenario, only one side of the contact has the surface oxide film. The existence of the surface oxide film attributes to the difference in the harmonic level and variation in these three contact scenarios.

4.2. CONTACT FORCE

The surface oxide film is more likely to break when subject to a higher contact force. The influence of contact force was studied. A range of 0.1 N to 1.4 N of contact force was tested for goldSpr-goldPad, susSpr-susPad and goldSpr-susPad. To avoid touching the same location on the landing pad, the spring was moved in y-axis for 0.1

mm for each contact force measurement, as illustrated in Figure 19. At each contact

location, 10 harmonic values were recorded for every 10 seconds. The results are

summarized in Figure 20. For all three contact scenarios tested, the average harmonic

shows a decreasing trend with increasing contact forces, which is as expected. For each

contact scenario (Figure 21, Figure 22 and Figure 23), the Box-Whisker plot is used here

to indicate the statistical characteristics of the harmonic generation.
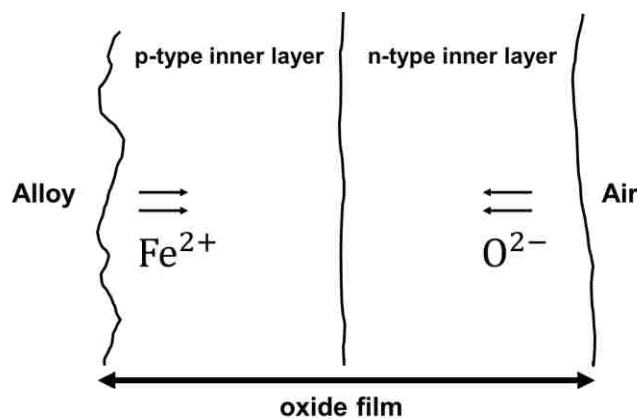
Figure 17. p-n junction formed on the stainless steel.
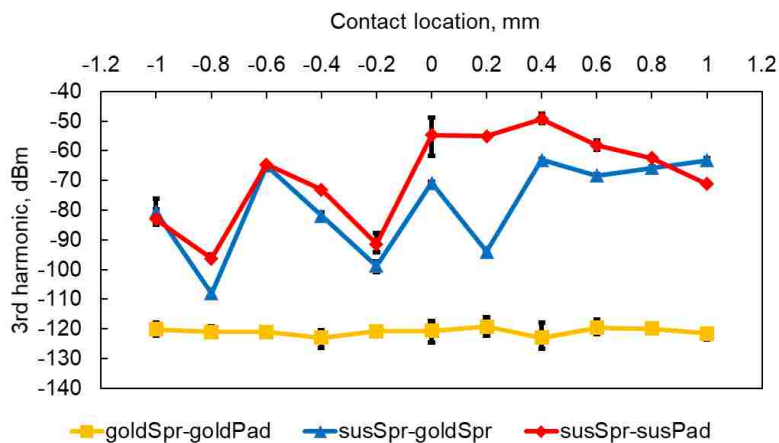
Figure 18. Comparison of different contact scenarios.
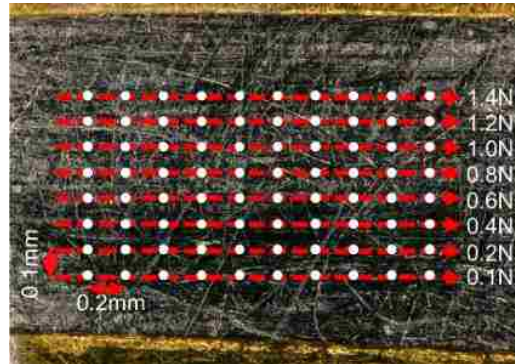
Figure 19. Test locations for the contact force vs harmonic measurement.

In the plot, for each data item, the upper error bar is the maximum value in the measurement, the lower error bar is the minimum value in the measurement, and the middle bar in the box is the mean value of the data. The upper bar of the box represents the 75% percentile while the lower bar of the box represents the 25% percentile, which means that 50% percent of the data falls into the box. For goldSpr-goldPad contact, the harmonic level remains very low value for all contact forces. The fluctuation of harmonic is also small. The susSpr-susPad contact has the highest harmonic level and the highest fluctuation. The average harmonic for goldSpr-susPad is between the susSpr-susPad and the goldSpr-goldPad. Although the harmonic at high contact force shows a much smaller value for susSpr-susPad comparing to the low contact force case, the fluctuation is still high. Thus, it is not feasible to improve the susSpr-susPad contact harmonic by simply increasing the contact force.

4.3. CONTACT RESISTANCE

The metal to metal contact usually has small contact resistance which is in mΩ range. However, when there are MIM junctions at the contact surface, the contact

resistance can rise to several Ωs. The contact resistance of the goldSpr-goldPad and

susSpr-susPad was measured by the Inductace-Capacitance-Resistance (LCR) meter, as

shown in Figure 24. The goldSpr-goldPad contact resistance is shown in Figure 25. The

contact resistance is below 45 mΩ, while the 3rd harmonic is below -120 dBm. On the

other hand, the susSpr-susPad contact shows the contact resistance in the range of 1 to 3

Ω (Figure 26). The high contact resistance is correlated to the high harmonic level.

Takeno [4] also reported a similar contact resistance range in his stainless-steel contact

study.
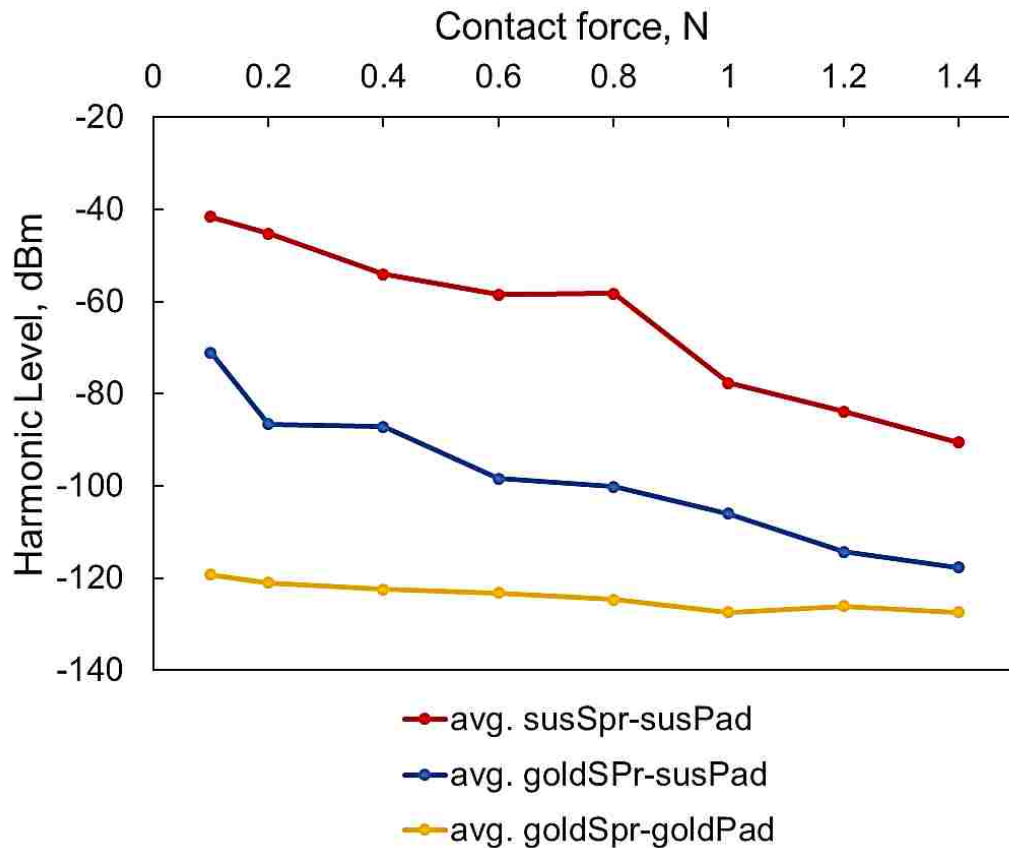
Figure 20. Comparison of the average 3rd harmonic vs contact force.
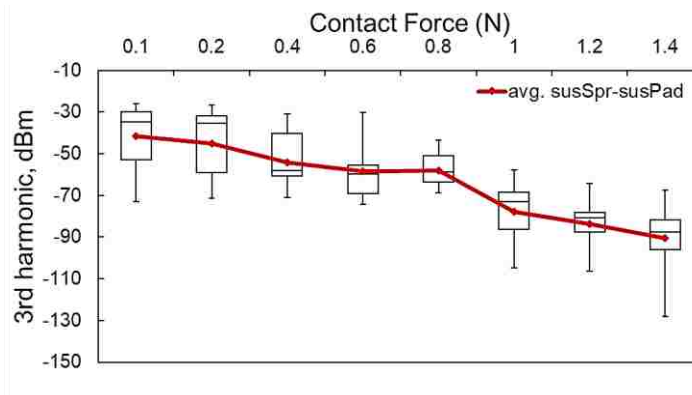
Figure 21. Box-Whisker plot for the 3rd harmonic vs contact force.
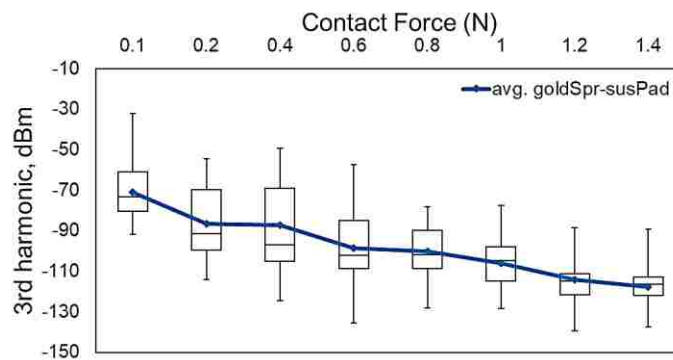
Figure 22. Box-Whisker plot for the 3rd harmonic vs contact force (gold-SUS contact).
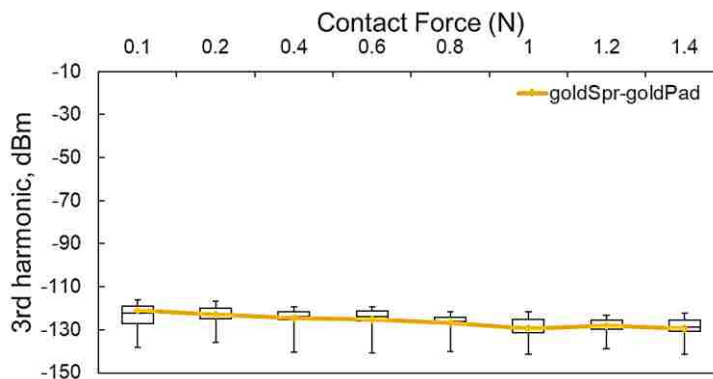
Figure 23. Box-Whisker plot for the 3rd harmonic vs contact force (gold contact).
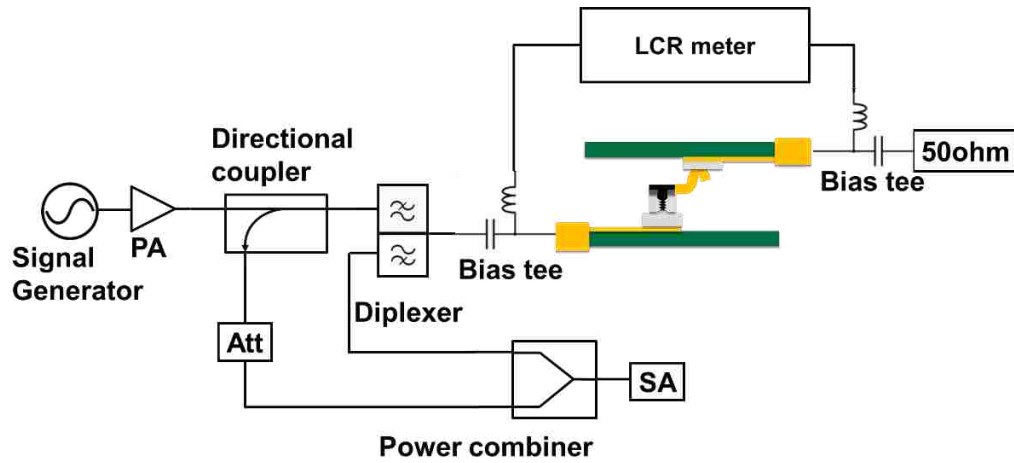
Figure 24. The 3rd harmonic vs contact resistance measurement setup.
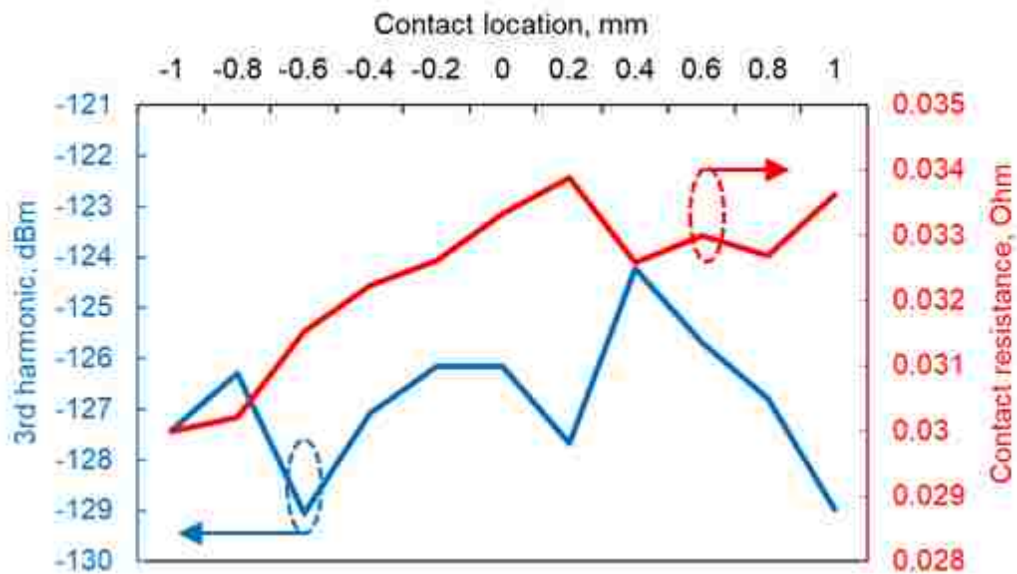
Figure 25. The 3rd harmonic vs contact resistance measurement result for goldSpr-goldPad contact.

5. DISCUSSION

The spring contact experiment has shown that the gold contact is much more superior than the stainless-steel contact, in terms of harmonic suppression. However, the

stainless-steel contact is desirable in the industry because of its lost cost. By increasing

the contact force, the harmonic generation of the stainless-steel contact can be greatly

reduced. However, the fluctuation of the harmonic is still high when there is a high

contact force. The high variation of harmonic will result in high failure rate in the product

and delay the product delivery. For the moment, the gold contact is still the best option

when considering the harmonic suppression, even though it has a higher cost per unit.
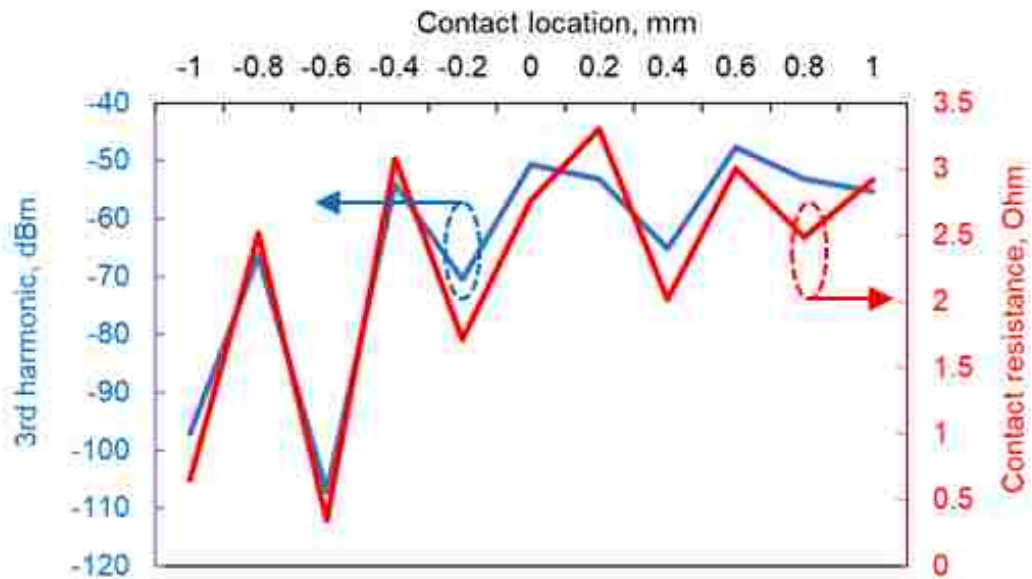
Figure 26. The 3rd harmonic vs contact resistance measurement result for susSpr-susPad contact.

6. CONCLUSION

The spring contact harmonic generation has been characterized experimentally in

the paper. The semiconductor-like junction is found to be the harmonic source at the

spring contact. The DC bias experiment shows interesting behavior which originates from

its semiconducting property. However, the exact mechanism is still unknown. Both MIM and p-n junction could exist at the contact junction. The gold contact has been proven to be much more superior than the stainless-steel contact in terms of harmonic suppression at the nominal contact force. There is strong correlation between high contact resistance and high harmonic level. When increasing the contact force, the overall harmonic generated at the stainless-steel contact reduces, however, the fluctuation of the harmonic is still high at large contact force. Thus, it is not possible to improve the stainless-steel contact harmonic generation by simply increasing the contact force.

REFERENCES

[1]   K. Hajek and J. Sikula, "Contact voltage of third harmonic distortion for contact reliability investigation," in IEEE Transactions on Components and Packaging Technologies, vol. 28, no. 4, pp. 717-720, Dec. 2005.

[2]   Holm, Ragnar. "The electric tunnel effect across thin insulator films in contacts." Journal of Applied Physics 22, no. 5 (1951): 569-574.

[3]   E. Takano, "Analyses on thin film between contacts by using third harmonic distortion," Proceedings of the Forth-Seventh IEEE Holm Conference on Electrical Contacts (IEEE Cat. No.01CH37192), Montreal, Que., 2001, pp. 192-196.

[4]   E. Takano, "Contact current distortion due to tunnel effect," Electrical Contacts - 2000. Proceedings of the Forty-Sixth IEEE Holm Conference on Electrical Contacts (Cat. No.00CB37081), Chicago, IL, USA, 2000, pp. 169-175

[5]   Kogut, L., and K. Komvopoulos. "Electrical contact resistance theory for conductive rough surfaces separated by a thin insulating film." Journal of applied physics 95.2 (2004): 576-585.

[6]   S. Yong et al., "Passive Intermodulation Source Localization Based on Emission Source Microscopy,", in IEEE Trans. Electromagn. Compat., to be published.

[7] X. Chen et al., "Analytic Passive Intermodulation Behavior on the Coaxial Connector Using Monte Carlo Approximation," in IEEE Trans. Electromagn. Compat., vol. 60, no. 5, pp. 1207-1214, Oct. 2018.

[8] X. Chen et al., "Coplanar Intermodulation Reference Generator Using Substrate Integrated Waveguide With Integrated Artificial Nonlinear Dipole," in IEEE Trans. Electromagn. Compat., to be published.

[9] S. Yang et al., "A passive intermodulation source identification measurement system using a vibration modulation method," IEEE Trans. Electromagn. Compat., vol. 59, no. 6, pp. 1677–1684, Dec. 2017.

[10] X. Chen and Y. He, "Reconfigurable passive intermodulation behavior on nickel-coated cell array," IEEE Trans. Electromagn. Compat., vol. 59, no. 4, pp. 1027–1034, Aug. 2017.

[11] A. Shitvov, A. Schuchinsky, and D. Zelenchuk, "Near-field mapping of passive intermodulation in printed circuits," in Proc. 4th Eur. Conf. Antennas Propag., Barcelona, Spain, 2010, pp. 1–4.

[12] International Standard: RF Connectors, Connector Cable Assemblies and Cables—Intermodulation Level Measurement, IEC Standard 62037, 1999.

[13] J. J. Henrie, A. J. Christianson and W. J. Chappell, "Linear–Nonlinear Interaction and Passive Intermodulation Distortion," in IEEE Transactions on Microwave Theory and Techniques, vol. 58, no. 5, pp. 1230-1237, May 2010.

[14] J. R. Wilkerson, K. G. Gard, A. G. Schuchinsky and M. B. Steer, "Electro-Thermal Theory of Intermodulation Distortion in Lossy Microwave Components," in IEEE Transactions on Microwave Theory and Techniques, vol. 56, no. 12, pp. 2717-2725, Dec. 2008.

[15] E. Rocas et al., "Passive Intermodulation Due to Self-Heating in Printed Transmission Lines," in IEEE Transactions on Microwave Theory and Techniques, vol. 59, no. 2, pp. 311-322, Feb. 2011.

[16] Henrie, Justin, Andrew Christianson, and William J. Chappell. "Linear-nonlinear interaction's effect on the power dependence of nonlinear distortion products." Applied Physics Letters 94.11 (2009): 114101.

[17] C. Vicente and H. L. Hartnagel, "Passive-intermodulation analysis between rough rectangular waveguide flanges," IEEE Trans. Microw. Theory Techn., vol. 53, no. 8, pp. 2515–2525, Aug. 2005.

[18] C. Vicente, D. Wolk, H. L. Hartnagel, B. Gimeno, V. E. Boria, and D. Raboso, "Experimental analysis of passive intermodulation at waveguide flange bolted connections," IEEE Trans. Microw. Theory Techn., vol. 55, no. 5, pp. 1018–1028, May 2007.

[19] DongWei Wu, Minfang Zhang, He Bai, Yongjun Xie, Liqiang Niu, Legen Dai, "An extraction method of MIM barrier voltage for PIM prediction on mesh reflector", Microwave and Millimeter Wave Technology (ICMMT) 2016 IEEE International Conference on, vol. 1, pp. 443-445, 2016.

[20] Bin Wang, Lijia Chen, Hua Zong, Jinghui Qiu, "The study on passive intermodulation research models", Mechatronic Sciences Electric Engineering and Computer (MEC) Proceedings 2013 International Conference on, pp. 3099-3103, 2013.

[21] PyVISA, 2016. [Online]. Available: https://pyvisa.readthedocs.io/en/master/#

[22] Ningshen, S., U. Kamachi Mudali, V. K. Mittal, and H. S. Khatak. "Semiconducting and passive film properties of nitrogen-containing type 316LN stainless steels." Corrosion science 49, no. 2 (2007): 481-496.

[23] Ferreira, M. G. S., M. Da Cunha Belo, N. E. Hakiki, G. Goodlet, M. F. Montemor, and A. M. P. Simões. "Semiconducting properties of oxide and passive films formed on AISI 304 stainless steel and alloy 600." Journal of the Brazilian Chemical Society 13, no. 4 (2002): 433-440.

[24] Lee, Jae-Bong, and Suk-Won Kim. "Semiconducting properties of passive films formed on Fe–Cr alloys using capacitance measurements and cyclic voltammetry techniques." Materials chemistry and physics 104, no. 1 (2007): 98-104.

[25] Hakiki, N. E., M. Da Cunha Belo, A. M. P. Simoes, and M. G. S. Ferreira. "Semiconducting properties of passive films formed on stainless steels influence of the alloying elements." Journal of the Electrochemical Society 145, no. 11 (1998): 3821-3829.

[26] Hakiki, N. E., M. F. Montemor, M. G. S. Ferreira, and M. da Cunha Belo. "Semiconducting properties of thermally grown oxide films on AISI 304 stainless steel." Corrosion science 42, no. 4 (2000): 687-702.

[27] Fujimoto, S., & Tsuchiya, H. (2007). Semiconductor properties and protective role of passive films of iron base alloys. Corrosion science, 49(1), 195-202.

II. DIFFERENTIAL E-FIELD COUPLING TO SHIELDED H-FIELD PROBE IN NEAR-FIELD MEASUREMENTS AND A SUPPRESSION APPROACH

ABSTRACT

In near-field scanning using H-field probes, E-field coupling is a major concern. E-field suppression performance must be characterized before an H-field probe can be used for near-field scanning. Common method of measurement involves measuring the E-field coupling in the same location where the strongest H-field coupling occurs. In microstrip line traces it is assumed that this occurs right above the center of the trace, and less coupling at all other locations across the microstrip line. In this paper we show that the maximum E-field coupling occurs at a location slightly offset from the trace center. The E-field coupling to a shielded H-field probe at such a position leads to differential mode coupling which the standard shield of an H-field probe is unable to suppress. The coupling mechanism is investigated and a differential E-field coupling suppression approach is proposed. For the H-field probe used in this work, a proposed floating plate is shown to improve the measured E-field suppression ratio by a factor of 18 dB compared to a similar probe without this modification.

1. INTRODUCTION

Near-field probes are developed to investigate electromagnetic compatibility and interference issues in electronic systems by measuring the electromagnetic fields radiated from the systems [1]-[8]. H-field probes are customarily used for this type of

investigation. Consequently, these H-field probes must be designed to have high

sensitivity [9]-[11] and provide good spatial resolution [12]-[16]. E-field coupling is a

major concern for H-field probe design since it leads to erroneous measured data in a

near-field scan. The E-field coupling to the H-field probe, under uniform E-field

distribution, was studied in [17]. Common-mode currents can be induced on the probe

shield, by the uniform E-field, and subsequently couple into the inner structure of the

shielded H-field probe (Figure). Analytical modeling, in conjunction with measurements,

have shown that the common mode E-field coupling can be significantly reduced when

the probe structure is symmetrical. However, when a complex structure is scanned in the

near-field of a probe, the assumption of a uniform E-field is no longer valid. A nearby

trace may contribute a strong non-uniform E-field at the probing location of the H-field.
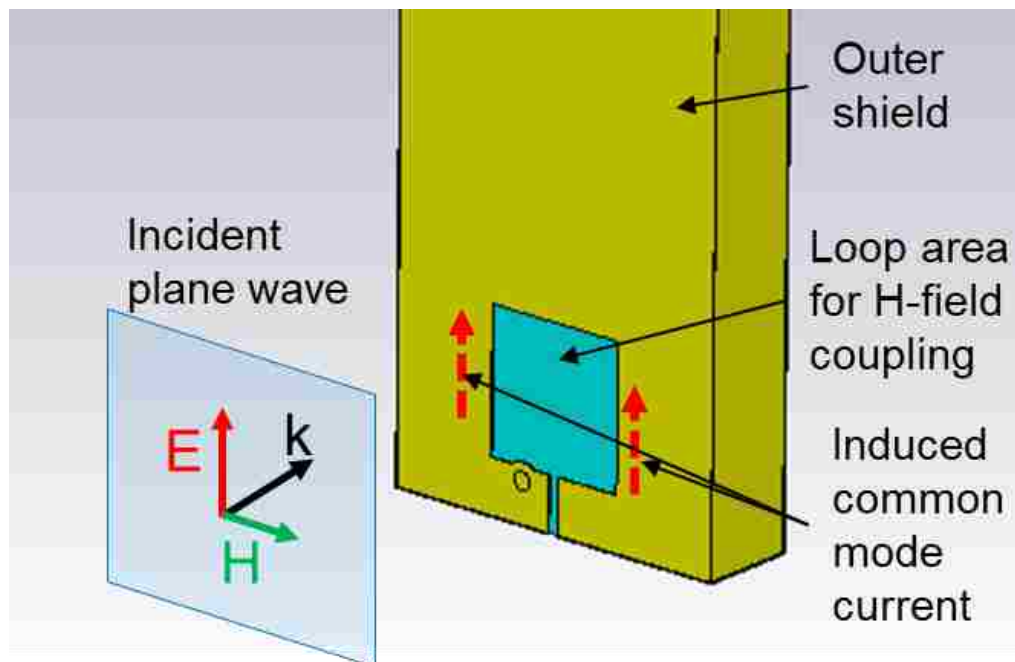
Figure 1. Illustration of uniform plane-wave inducing common-mode current on an H-field probe.
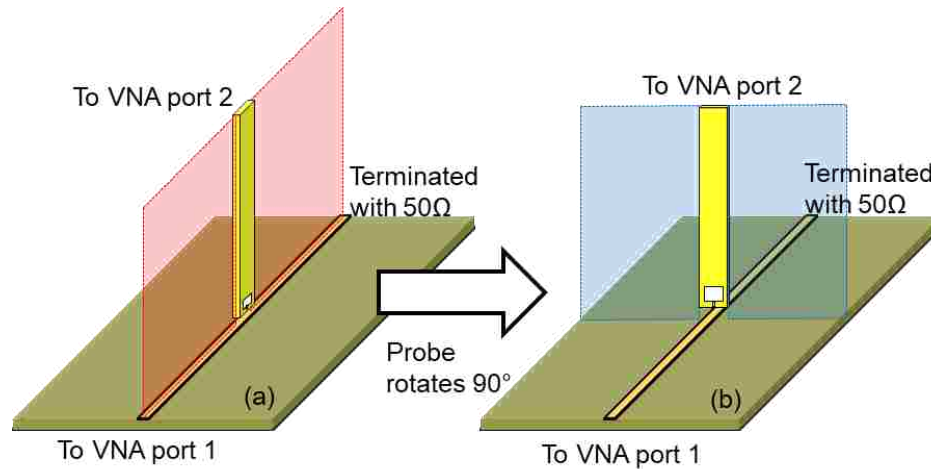
Figure 2. Typical: (a) H-field and (b) E-field characterization set-up.

A typical probe characterization procedure includes the following two steps [18][19]. Firstly, for measuring the desired coupled H-field component the probe is placed directly above the center of a microstrip trace (Figure 2 (a)), which is matched at one end, is connected to one port of the Vector Network Analyzer (VNA) at the other end. Then, the desired H-field coupling is characterized by the measured $|S_{21}|$. Secondly, to determine the suppression level of the unwanted field components, the probe is rotated by 90°, maintaining its position above the center of the trace (Figure 2 (a)). This results in the probe loop becoming parallel to the primary magnetic field such that this component cannot couple into the loop. The remaining coupling is then considered to be due to the E-field. The E-field rejection ratio is subsequently defined as the ratio of the magnitude of E- and H-field (H/E), at the same location.

The microstrip field may contain H-field components in the propagation direction, where it can couple into the loop area (Figure) if the loop plane is oriented parallel to the trace. This does not properly characterize the E-field coupling. As shown in Figure 3, the

E-field is axially symmetric about the z-axis. The typical E-field coupling measurement

position of an H-field probe is indicated by the dashed lines. The E-field coupling to the

H-field probe at this position is essentially common-mode coupling. Thus, it can be

greatly reduced by a highly symmetrical outer shield. However, as demonstrated in this

paper, the highest level of E-field coupling to the H-field probe actually occurs at the

edges of the trace, and not at the trace center. Thus, the worst-case E-field coupling is not

captured at the position mentioned in [16][18][19].
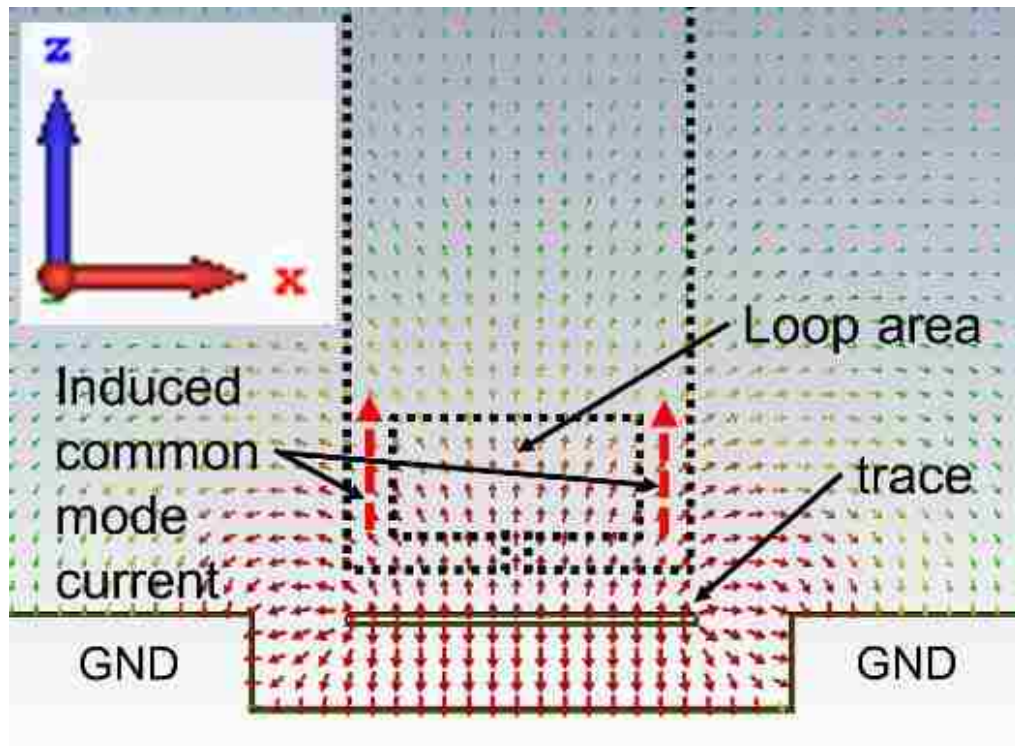
Figure 3. Cross-sectional E-field distribution above an air CPWG.

To overcome the deficiencies in the characterization process outlined in

[16][18][19]., a two-step procedure must be followed, namely: *i*) the field-generating

structure must only support a TEM mode, which can be achieved by using an air

insulated microstrip structure, and *ii*) the maximum E-field coupling position must be determined by scanning the probe across the microstrip line structure. As will be demonstrated later, the real maximum E-field coupling position is usually the edges of the trace. Therefore, instead of defining H/E ratio at the same location, it is necessary to redefine the E-field suppression ratio (H/E ratio) as the ratio of the maximum H-field (H_{max}) over the maximum E-field (E_{max}), H_{max}/E_{max}, while the probe is moved across the open tx-line structures.

The E-field coupling mechanism at such a position (trace edge) is essentially differential-mode coupling, which has not been reported in the existing literature. In this work, the differential E-field coupling mechanism is studied and an equivalent circuit is proposed for a better understanding of this phenomenon. A differential E-field coupling suppression method is proposed as well, which requires only a relatively simple, yet effective, modification to the existing H-field probes. We will show this method to be capable of achieving 18 dBs of measured improvement in E-field suppression. General considerations for the H-field probe design for high-frequency applications (above 10 GHz) are discussed, as well.

2. NON-TEM FIELD COMPONENTS IN OPEN TRANSMISSION LINE STRUCTURES

In microstrip lines, and co-planar waveguides (CPWG) (i.e., open structures) propagation velocities in the air and in their dielectric substrates are different. Therefore, only quasi-TEM (transverse electromagnetic) mode can be established in the dielectric-substrate and not an ideal TEM mode. Consequently, as the frequency increases, the non-

TEM field components in the quasi-TEM wave may no longer be ignored. When using dielectric-substrate CPWG or microstrip for E-field coupling characterization (Figure 2 (b)) of a probe, the non-TEM component results in incorrect E-field suppression data.

To investigate the effect of non-TEM component above the open transmission line (tx-line) structures, two types of CPWGs, one with air as its substrate, and the other with Roger's RO4350B substrate are simulated using CST Microwave Studio®, as shown in Figure 4. To simplify the model and to reduce simulation time, the ground of CPWG is modeled as a copper block with a cut-out slot. The dimensions of the CPWGs are optimized to ensure 50 Ω characteristic impedance. The cross-sectional dimensions are shown in Figure 4. The TEM field components in these models are Ex, Ez, Hx, and Hz, while the non-TEM field components are Ey and Hy. For the air (vacuum) substrate CPWG, the TEM mode is expected because the medium is homogeneous. On the other hand, quasi-TEM is the dominant mode in the CPWG with the dielectric-substrate. The field data at 10 GHz are recorded in the simulation. The coupling position of E- and H-field to the probe tip is different. The E-field coupling usually happens at the bottom of the tip while the H-field coupling happens at the loop area. Thus, it is necessary to investigate the E- and H-field separately instead of plotting the field at the same position. The E-field magnitude (Figure 5) is plotted at the height of the probe bottom (1 mm above the CPWG as shown in Figure 4 (a)), typical for this type of EMC (Electromagnetic Compatibility) measurements. The H-field magnitude (Figure 6) is plotted at the height of the loop area center of the probe (2.8 mm above the CPWG as shown in Figure 3(b)). As shown in Figure 5, at 10 GHz, the maximum non-TEM component Ey is 33 dB lower than that of the TEM components. On the other hand, the

maximum non-TEM component of the H-field Hy is only 11 dB lower than the maximum

TEM H-field component H_x (Figure 6). When the H-field probe is rotated 90° to measure

E-field coupling, the non-TEM H-field component (H_y) couples to the probe. As a result,

only 11 dB E-field suppression is achieved by an ideal H-field probe at 10 GHz, when

placing the probe bottom 1 mm above the trace. This is likely attributed to the non-TEM

H-field component in the dielectric substrate, having an adverse impact on the E-field

coupling characterization measurement.
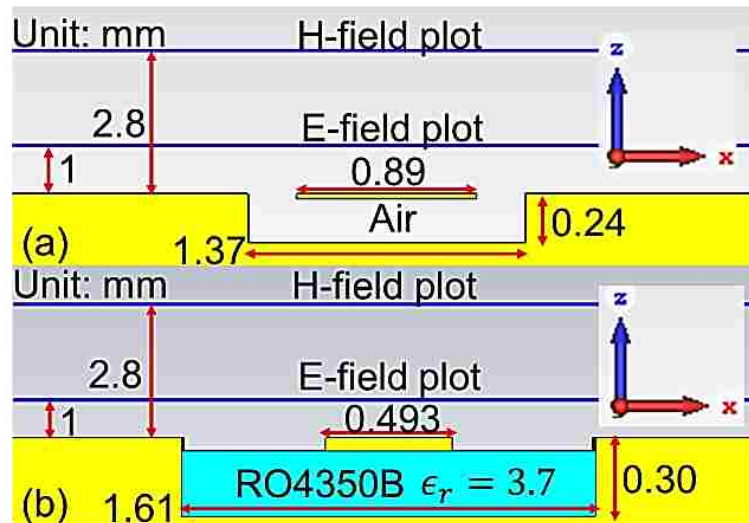
Figure 4. Cross section of CPWG models in CST.

To avoid any non-TEM H-field components caused by the dielectric substrate an

air substrate microstrip structure (Figure 7) is built for the E-field coupling measurement.

The trace is 3 mm wide and 0.5 mm above the ground. One end of the trace is soldered to

the inner conductor of an SMA connector; the other end is terminated with two in parallel

100 Ω 0603 resistors. There is no supporting structure between the two ends so that the

homogeneous medium for TEM mode is guaranteed. The TDR measurement showed that

the impedance variation of the air microstrip structure is within 50±3 Ω, and the

measured $|S_{11}|$ is below -10 dB for the frequency up to 11 GHz.
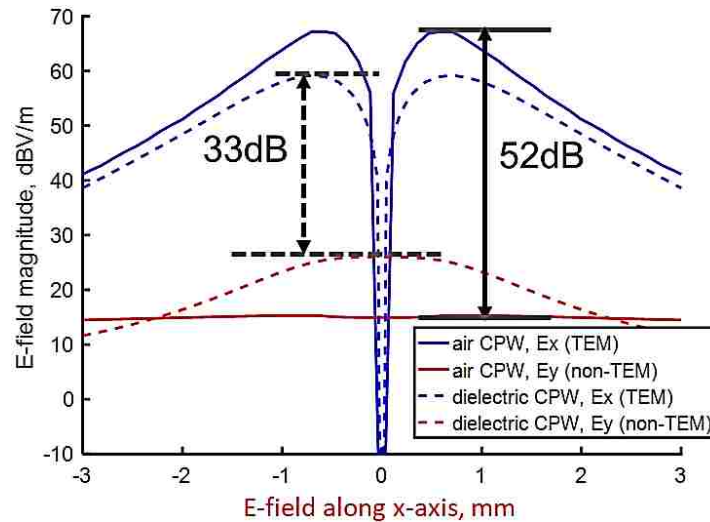
Figure 5. Simulated E-field distribution comparison.
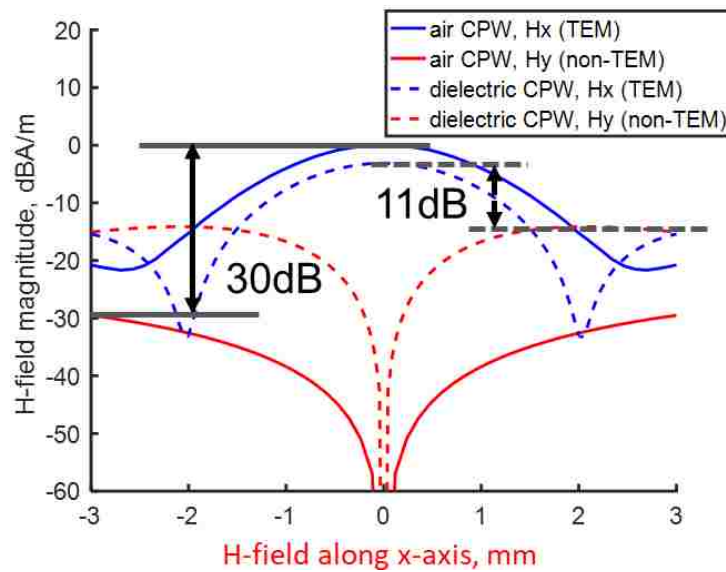
Figure 6. Simulated H-field distribution comparison.
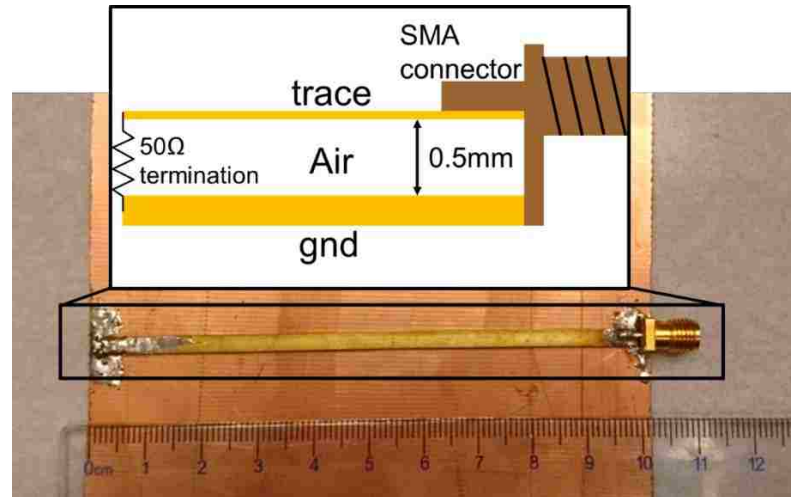
Figure 7. Air substrate microstrip trace.

3. DIFFERENTIAL E-FIELD COUPLING TO H-FIELD PROBES

In the previous studies, the E-field coupling is measured by rotating the probe 90° at the same position as the H-field measurement (Figure 2). By rotating the probe 90°, there is very limited magnetic flux penetrating through the loop area. Thus, at this angle only E-field coupling will be measured in the air portion of the structure.

Although the field distribution above the PCB is non-uniform, the cross-sectional E-field is axially symmetric about the z-axis (Figure 3). Thus, the E-field coupling measured by rotating 90° at the H_{max} position is still common-mode to the H-field probe. Therefore, by making the probe highly symmetrical and making additional shielding structures, excellent E-field suppression performance can be achieved [16][18][19].

However, our experiments and simulations have shown that the position of E_{max} from an open tx-line structure, such as CPWG and microstrip, is slightly offset from the H_{max} position (the trace center).

In this section, the design details of the H-field probe used in the measurements is first introduced. The measurement set-up and the measured results are also shown. Full-wave simulations are performed for the investigation of the E-field coupling. Finally, an equivalent circuit is proposed to illustrate the differential E-field coupling mechanism.

3.1. BROAD-BAND H-FIELD PROBE

Detailed stack-up and dimensions of the H-field probe used in this work are shown in Figure 8. The probe is built on a four-layer MEGTRON6 (DK = 3.72, DF = 0.002) PCB with plated edges, which form a shielding enclosure. An L-shaped stripline is implemented as the signal trace which connects to the outer shield with a plated via. Two loop areas are placed on the top and bottom layers as the H-field coupling paths. Figure 9 shows a tapered design for the transition from stripline to CPWG. The variation of the transmission line characteristic impedance is within ±1.5 Ω, measured by a TDR, as shown in Figure 9.
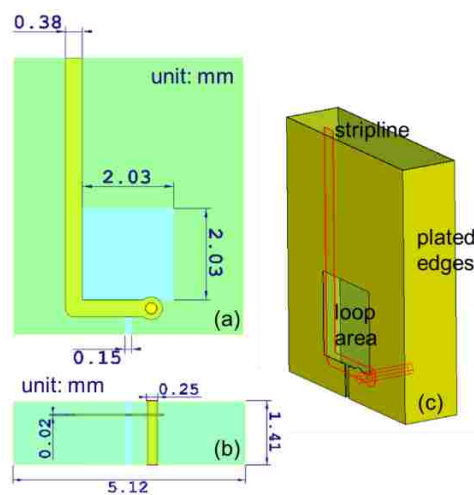
Figure 8. Stack-up and dimensions of the H-field probe tip.
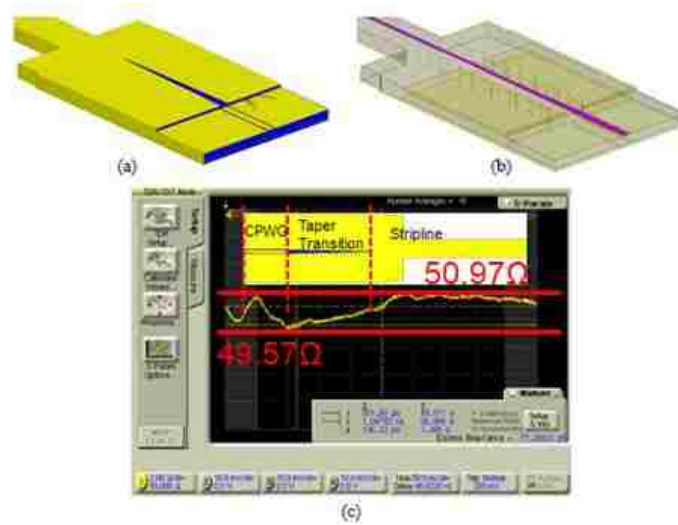
Figure 9. Taper designs for the transition from stripline to CPW.

3.2. PROBE CHARACTERIZATION

The probe was characterized for H-field coupling by scanning above the

microstrip trace (Figure 10)). The microstrip trace was excited by signals from port 1 of

the VNA (Figure 10). The H-field probe was connected to port 2 of the VNA. The probe

position was controlled using a computer-controlled near-field scanning apparatus.
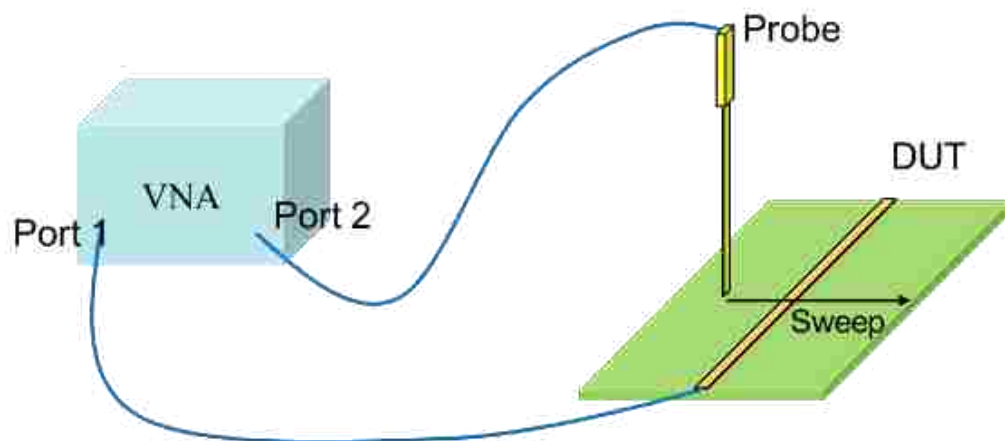
Figure 10. Measurement set-up for E- and H-field coupling to the H-field probe.

The probe scanned across the trace along an observation line, as shown in Figure 11. The H- and E-field coupling measurement results at 5 GHz and 10 GHz, are shown in Figure 12, respectively. As the probe moves away from the trace center, the amplitude of the horizontal component of the H-field (H_x) decreases. Two minima occur at both sides of the trace because at such position the H_z component is the strongest, which cannot couple to the loop. As for the E-field coupling (Figure 11 (b)), two symmetrical maxima were observed in $|S_{21}|$, on both sides of the trace, which corresponds to the edges of the microstrip trace. At the height of 1 mm, the peak value is 8 dB lower than the peak value of H-field coupling at 5 GHz. At the same height, the peak magnitude of E-field coupling is 4.5 dB higher than that of H-field coupling at 10 GHz. This shows that E-field couples more significantly to the H-field probe at high frequencies, which would result in measurement error if care is not taken in this situation. As shown in Figure 13, the max-E coupling becomes comparable to max-H coupling after 6.5GHz.
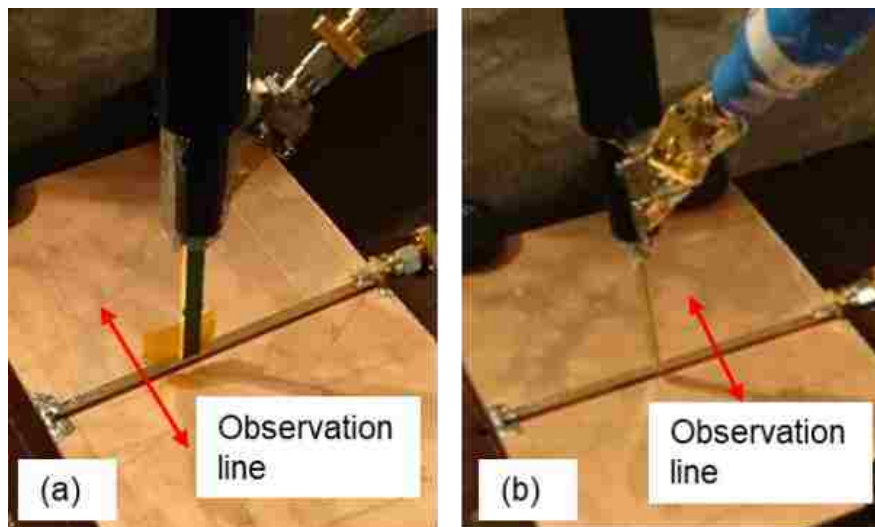
Figure 11. Measurement set-up to characterize H-field probe.
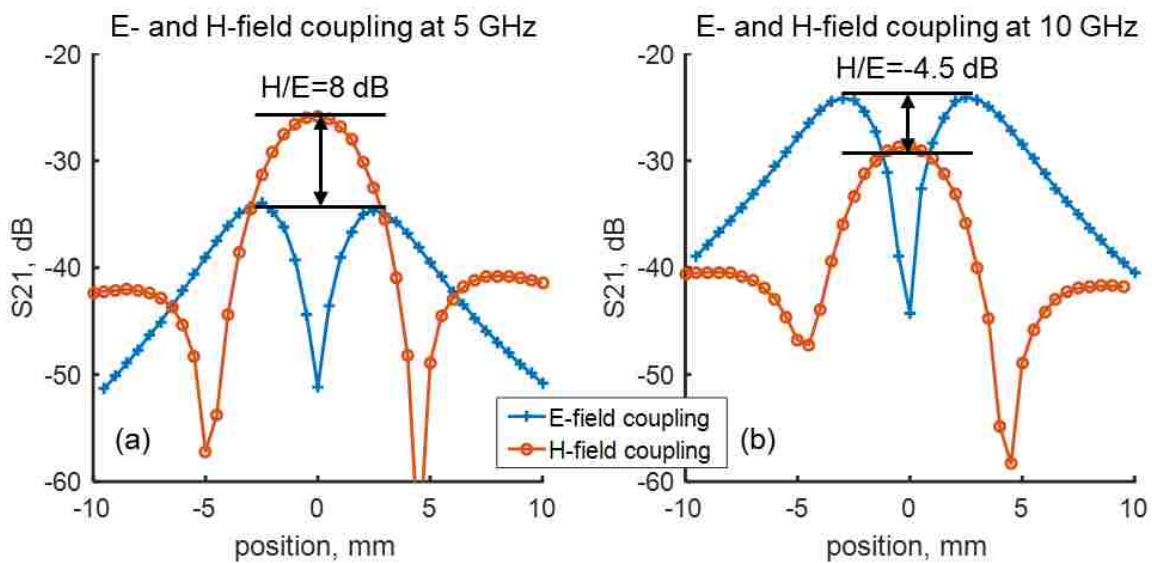
Figure 12. Measured E- and H-field coupling of the probe.
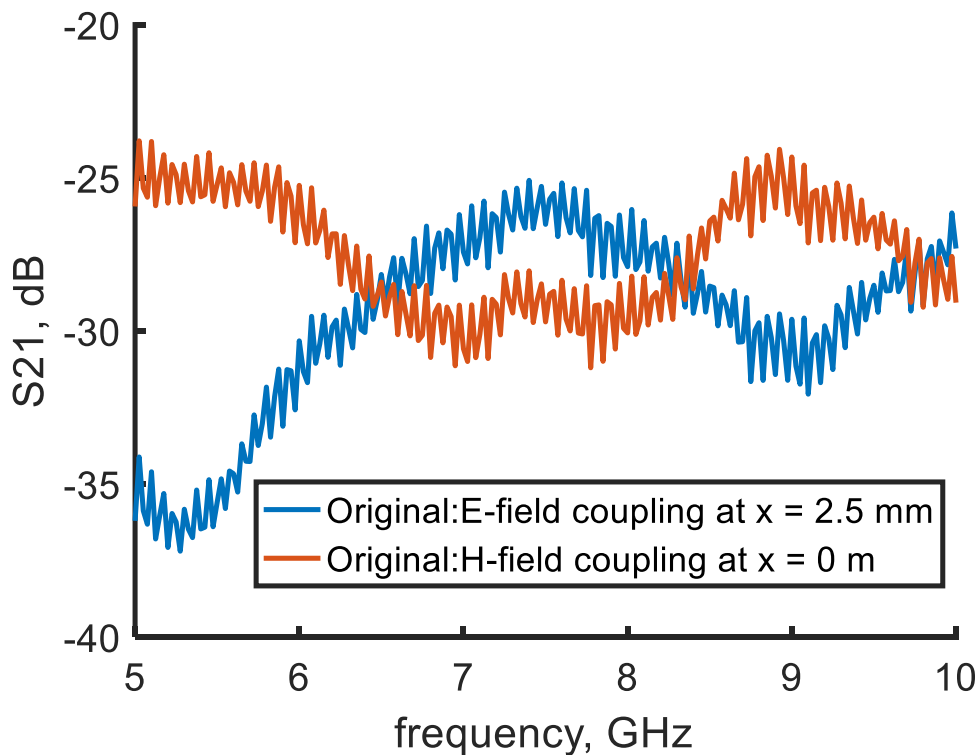
Figure 13. S_{21} comparison of max E-field and max H-field coupling.

3.3. DIFFERENTIAL E-FIELD COUPLING MECHANISM

Full-wave simulations were performed to investigate E-field coupling mechanism (Figure 14). The air CPWG structure (Figure 4 (a)) was used in the simulation. The CPWG structure has stronger E-field coupling to the H-field probe than the microstrip structure since its ground is closer to the probe bottom than the microstrip structures. The probe bottom is 1 mm above the trace which is the same as in the measurement.

As shown in Figure 15, compared with the E_{max} in the measurement (Figure 12), similar behavior is observed in the simulation: The E_{max} position occurs right above the gap between CPWG's trace and ground, rather than in the trace center. The E_{max} is 10 dB higher than the H_{max} at 10 GHz.

A closer look into the probe bottom structure reveals the mechanism of differential E-field coupling (Figure 16 and Figure 17). The right-hand side of the probe bottom forms a capacitance to the ground while the left-hand side forms a capacitance to the trace, as indicated by $C_{1,trace}$ and $C_{2,gnd}$ in Figure 17 and Figure 18. Large potential differences are formed across the slot at the probe bottom. This is essentially a differential coupling mechanism. Thus, all the approaches that have been previously taken for common-mode E-field coupling suppression will fail to suppress this differential E-field coupling mechanism.

An equivalent circuit model was created to help understand the E-field coupling of the H-field probe, as shown in Figure 18. The source driving the CPWG trace is represented by the voltage source V_s in series with source impedance Z_s. The entire CPWG trace is only represented with the source impedance Z_s and load impedance Z_L, because the CPWG characteristic impedance was designed to match both the source and

load impedances. Capacitance $C_{1,trace}$ represents the E-field coupling from the CPWG

trace to the left-hand side of the probe while $C_{2,gnd}$ is the capacitance from CPWG ground

to the right-hand side of the probe shield. The slot capacitance was ignored because it

was estimated to be insignificant. Differential voltage is induced on the slot input

impedance Z_{12} when the displacement current flows through the capacitive coupling path

of trace- $C_{1,trace}$ - Z_{12}- $C_{2,gnd}$ -gnd. The method to suppress the asymmetric E-field

coupling will be discussed in next section.
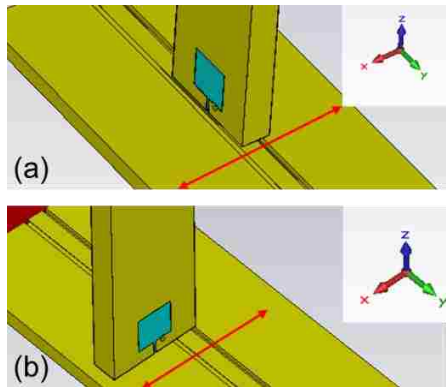
Figure 14. H-field coupling simulation.
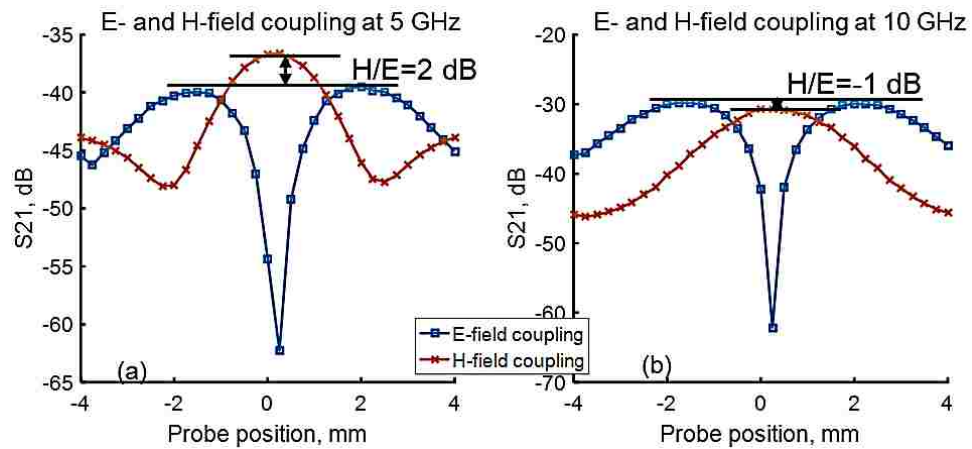
Figure 15. Simulated E- and H-field coupling.
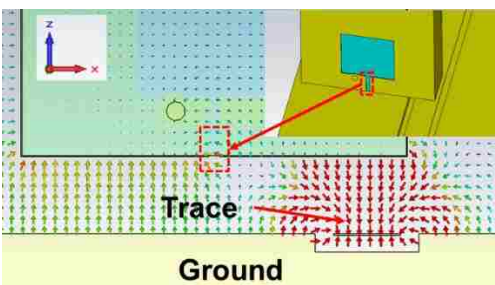
Figure 16. Cross-sectional E-field distribution.
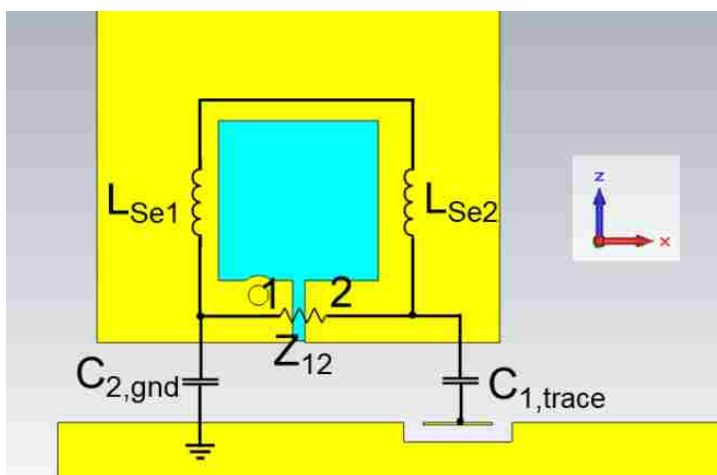
Figure 17. Full-wave model of the H-field probe.
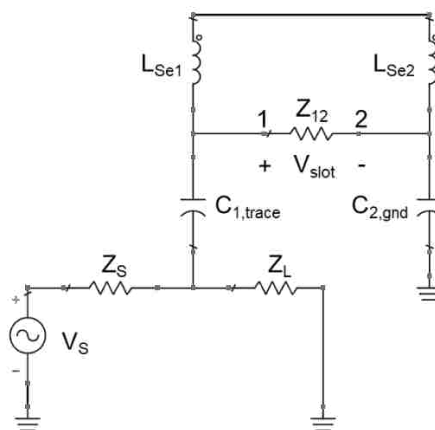
Figure 18. Equivalent circuit model of electric field coupling of H-field probe.

4. FLOATING PLATE METHOD FOR SUPPRESSION OF DIFFERENTIAL E-FIELD COUPLING

As discussed in the previous section, the E-field coupling at the trace edges is essentially differential-mode coupling, which is the same as the H-field coupling. Thus, it is impossible to reduce such coupling by previously reported methods such as improving the symmetry of the probe outer shield ([16]-[19].), or using differential loop [10]. The differential E-field coupling is unavoidable in the real EMC/RFI near-field measurement environments. A differential E-field suppression method is needed to ensure correct H-field measurement at higher frequencies. In this section, a differential E-field suppression method is introduced. One of its advantages is that it only slightly modifies the existing high-frequency H-field probes. The proposed method is not limited to the specific H-field probe, but it is applicable to a broad range of H-field probe design. The design guide for optimizing the proposed structure is introduced in the last part of this section so that the readers can optimize the proposed structure for their H-field probe designs for differential E-field suppression.

4.1. FLOATING PLATE STRUCTURE

The differential E-field coupling to the H-field probe is through a capacitive path, as illustrated in the previous section (Figure 17 and Figure 18). Intuitively, it is possible to reduce the differential E-field coupling by forcing the capacitance symmetry on either side of the slot. The floating plate method is proposed here based on this idea. A metal plate is inserted between the probe bottom and the CPWG (Figure 19). It is not connected to either the probe or the CPWG. The dimensions (width W, length L and the gap

between the probe bottom and the plate) of the floating plate are determined by the

parameter sweep shown in the part E of this section. The dimensions are W=1.9 mm,

L=5.17 mm, which means that the floating plate is slightly larger than the dimensions of

the probe bottom. The gap between the probe bottom and the floating plate is H=0.076

mm.
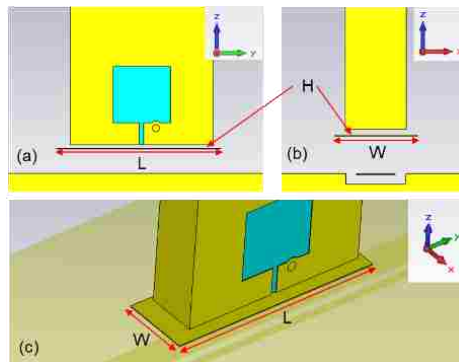
Figure 19. Floating plate under probe bottom for differential E-field suppression.

4.2. SIMULATION RESULTS

A copper plate was added between the probe bottom and CPWG in the full-wave

model. The floating plate is 0.762 mm below the probe bottom. The H-field probe with

floating plate is simulated along the observation line as shown in Figure 14. Figure 20 is

the combined results of H- and E-field coupling at 5 GHz and 10 GHz, with the probe

bottom 1 mm above the trace. It should be noted that the E_{max} position has been change to

Figure 22, from the position in Figure 17. Compared with the original design, the H/E

ratio has been improved by 13 dB at 10 GHz. The floating plate method shows excellent

improvement in the E-field suppression. The comparison of $|S_{21}|$ at the H_{max} (the trace

center) and the E_{max} (Figure 22) positions are shown in Figure 21. Significant E-field

coupling suppression was observed for all frequencies below 10 GHz.
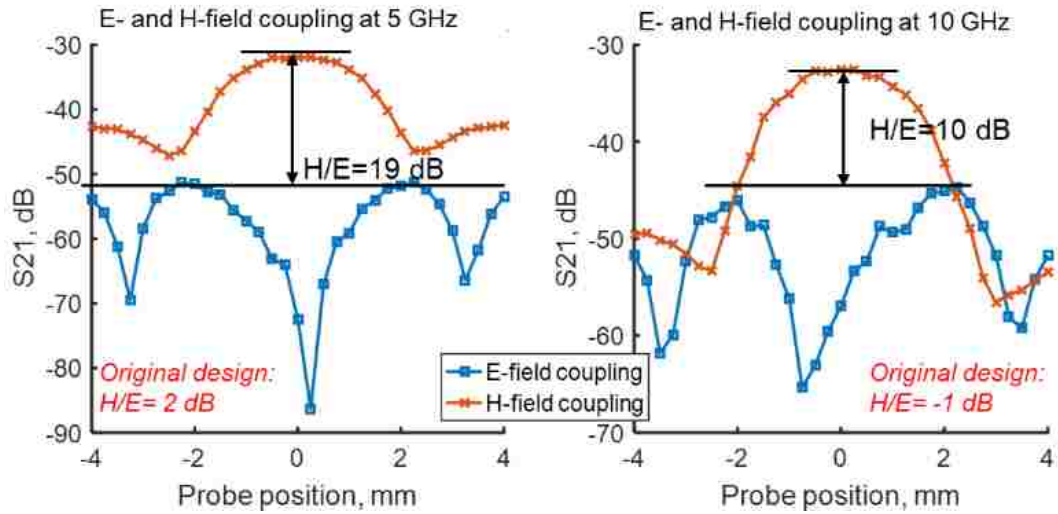
Figure 20. Simulated H- and E-field coupling for H-field probe added with floating plate.
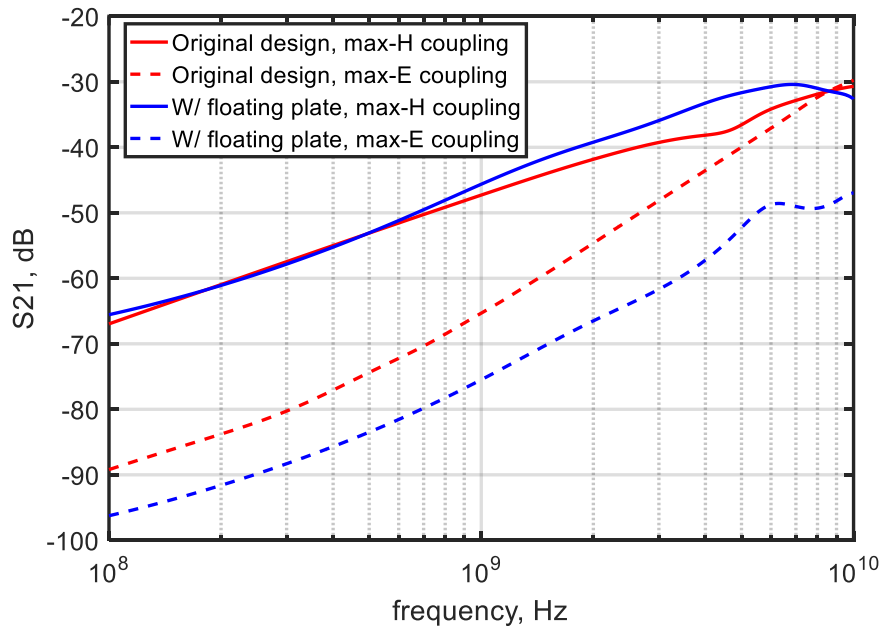
Figure 21. S_{21} comparison of H-field coupling and E-field coupling simulation results.

4.3. EQUIVALENT CIRCUIT

The floating plate is essentially a series capacitor between the probe and CPWG. The equivalent circuit is shown in Figure 22. and Figure 23. Most displacement current flows through the capacitive current path of trace-$C_{plate,trace}$-$C_{plate,gnd}$-gnd because that it has the least impedance comparing to other current paths. The unbalanced impedances of the current path trace-$C_{plate,trace}$ -$C_{1,plate}$–L_{Se11}-$C_{1,gnd}$-gnd and trace-$C_{plate,trace}$-$C_{2,plate}$-L_{Se21}-$C_{2,gnd}$ -gnd contribute to the current that flows through the input impedance of the slot, the differential noise voltage (V_{slot} in Figure 23) is, thus, induced on Z_{12}.

4.4. MEASUREMENT RESULTS

Based on the simulation results and equivalent circuit analysis, a modification was made to the H-field probe (Figure 24). The floating plate is made from a piece of copper tape. The simulation used an air space between the floating metal plate and the probe, while the measurement uses Mylar tape to hold the floating plate. For that reason, the simulation only shows the principle effects. Three layers of Mylar tape were inserted between as the spacer. The dielectric constant of the Mylar tape is about 2, and since it is very thin, any effect it may have on the measurements is expected to be negligible. It will be shown in the measurement results that the proposed method is effective in reducing the unwanted E-field coupling, thus, it is in line with the prediction by simulation. The gap between the copper plate and the probe is about 0.13 mm. The copper plate is about 1 mm wider than the probe bottom width and 0.5 mm longer than the probe bottom length.
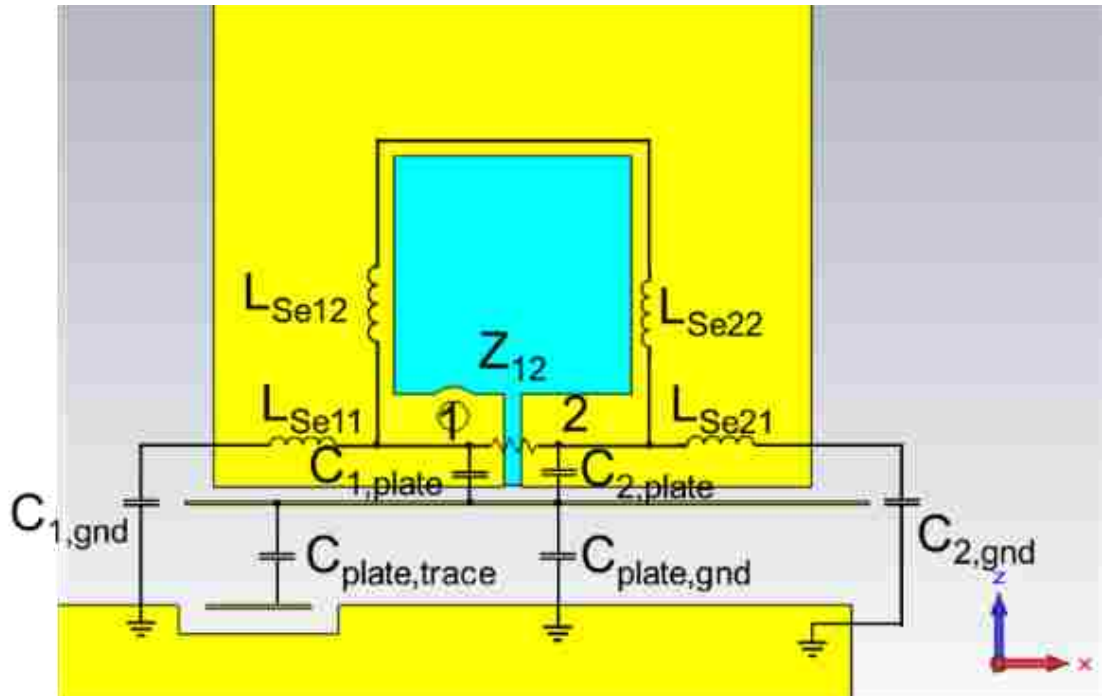
Figure 22. E$_{max}$ position after adding the floating plate.
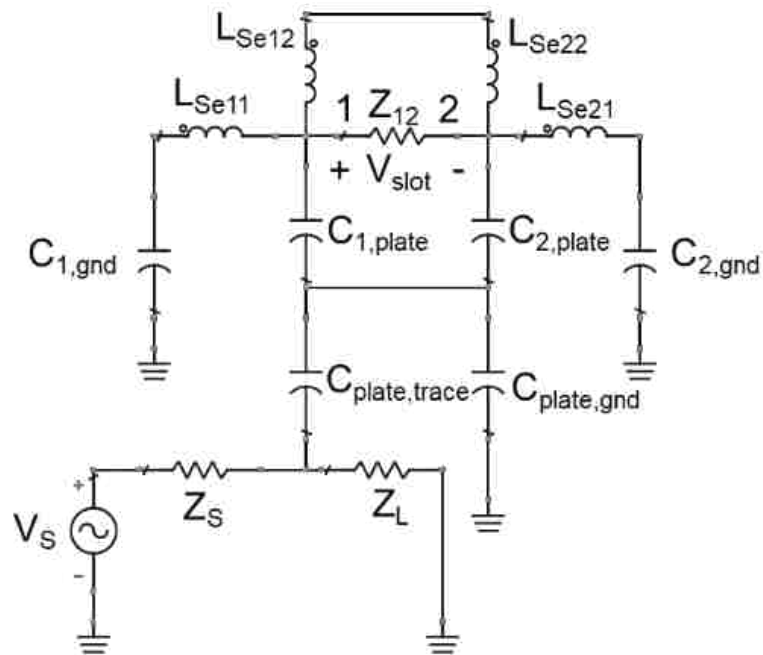
Figure 23. Equivalent circuit for E-field coupling of H-field probe with floating plate.

Figure 24. Floating plate made from copper tape.

The same measurement set-up in Figure 11 was used for E-field and H-field coupling measurement of the modified H-field probe. The results are summarized in Figure 25 and Figure 26. The H_{max} is now 13.6 dB higher than the E_{max}, comparing to -4.5 dB H/E ratio in the original design. Significant H/E ratio improvement (18 dB) is achieved by the floating plate method. The floating plate made from copper tape is not perfectly symmetric, and it is still effective in reducing the E-field coupling at all locations across the trace. This fact again verifies that the E-field coupling at the trace edges is differential mode, which means that it is impossible to suppress the E-field coupling at trace edges by making the probe highly symmetric.

4.5. DESIGN OPTIMIZATION

The simulation results indicate that the parameter W and L are correlated. It is impossible to sweep W and L separately and determine the optimal combination of W and L. Furthermore, the E_{max} position often changes when the W and L combination is

changed. Thus, for each W and L combination, it is necessary to sweep across the CPWG

as shown in Figure 13(b) to determine the E_{max} value. Generally, for all positions across

the CPWG, the E-field coupling magnitude increases with frequency. To speed up

simulation time, it is recommended to use a frequency solver in full-wave simulation and

only simulate at the highest operation frequency point (e.g., 10 GHz for the probe model

in this work). The H/E ratio at 10 GHz is selected as the criteria for parameter

optimization. The optimal W and L combination is selected as W=2.41 mm and L=6.11

mm. The E- and H-field coupling across the CPWG is shown in Figure 20.
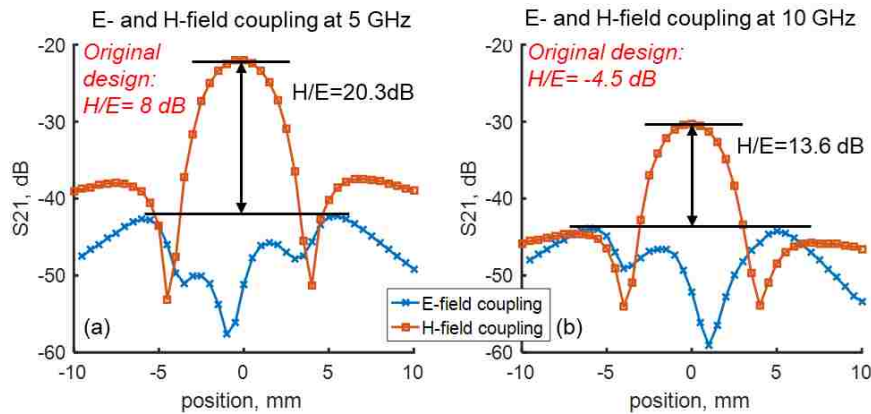
Figure 25. Comparison of the proposed method and the original design.

5. HIGH-FREQUENCY H-FIELD PROBE DESIGN CONSIDERATIONS

The differential E-field coupling to the shielded H-field probe for the frequencies

above 10 GHz can attribute to erroneous measurement data in a near-field scan. The

probe designers and probe users must pay attention to the differential E-field coupling

problem, which is generally much severe in the higher frequency range (above 7 GHz). It

is shown that by properly designing a probe and the measurement set-up, it is possible to avoid differential E-field coupling or at least expose the problem before deploying the probe into the real near-field measurement. Based on the findings in this paper, the authors would recommend following procedures for reducing differential E-field coupling problem.
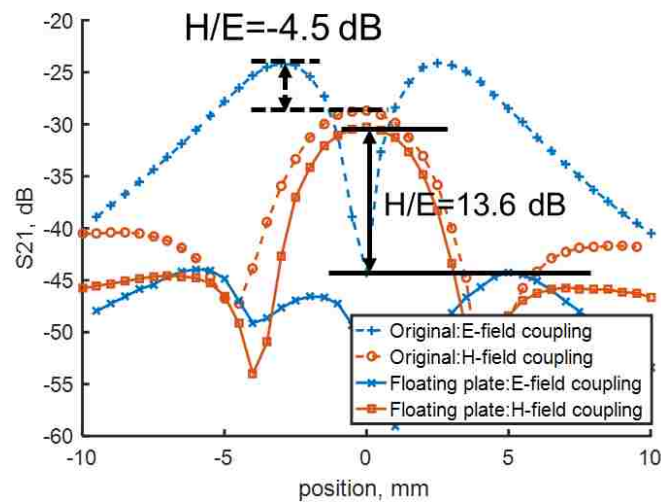
Figure 26. Comparison of E- and H-field coupling.

Use air substrate CPWG/microstrip for probe characterization in both simulation and measurement. The existence of the non-TEM field components on the dielectric-substrate tx-lines can lead to false H/E ratio.

Simulate multiple probe positions across the trace. The E_{max} has been shown not to be in the center of the trace, which indicates that by simply rotating the probe 90° for E-field coupling measurement is not sufficient.

Use the floating plate method and optimize its dimensions to achieve the best H/E ratio.

The authors believe that by reducing the loop area dimensions and the overall size of the probe tip, combined with the floating plate method, differential E-field suppression can be improved. Extensive simulation is needed before one could find out the optimal design for the H-field probe that operates above 10 GHz. It might be challenging to design a high-frequency H-field probe with good H/E ratio.

6. CONCLUSION

Differential E-field coupling to H-field is investigated in this work. It is shown that the E_{max} occurs at a different location other than that of the H_{max}, which contradicts the typical method of simply rotating the probe by 90° for the E-field coupling measurement (Figure 2). Ignoring the differential E-field coupling phenomenon can result in false measurement data in the near scan measurement. The floating plate method is proposed in this work to suppress the differential E-field coupling. Only slight modification is needed for the current existing H-field probes to adopt this method. The measurement results have shown that the proposed method can improve the H/E ratio for 18 dB at 10 GHz for the H-field probe used in this work.

REFERENCES

[1]   D. Baudry, C. Arcambal, A. Louis, B. Mazari and P. Eudeline, "Applications of the Near-Field Techniques in EMC Investigations," in *IEEE Transactions on Electromagnetic Compatibility,* vol. 49, no. 3, pp. 485-493, Aug. 2007.

[2]   J. Zhang, K. W. Kam, J. Min, V. V. Khilkevich, D. Pommerenke and J. Fan, "An Effective Method of Probe Calibration in Phase-Resolved Near-Field Scanning for EMI Application," in IEEE Transactions on Instrumentation and Measurement, vol. 62, no. 3, pp. 648-658, March 2013.

[3]   T. Dubois et al., "Near-Field Electromagnetic Characterization and Perturbation of Logic Circuits," in IEEE Transactions on Instrumentation and Measurement, vol. 57, no. 11, pp. 2398-2404, Nov. 2008.

[4]   Z. Yan, J. Wang, W. Zhang, Y. Wang and J. Fan, "A Miniature Ultrawideband Electric Field Probe Based on Coax-Thru-Hole via Array for Near-Field Measurement," in IEEE Transactions on Instrumentation and Measurement, vol. 66, no. 10, pp. 2762-2770, Oct. 2017.

[5]   G. Shen et al., "Maximum Radiated Emissions Evaluation for the Heatsink/IC Structure Using the Measured Near Electrical Field," in IEEE Transactions on Electromagnetic Compatibility, vol. 59, no. 5, pp. 1408-1414, Oct. 2017.

[6]   Q. Huang et al., "MoM based current reconstruction using near-field scanning," 2017 IEEE International Symposium on Electromagnetic Compatibility & Signal/Power Integrity (EMCSI), Washington, DC, 2017, pp. 549-554.

[7]   G. H. Li, W. Huang and D. Pommerenke, "Effect of cooling on the probe system sensitivity for low signal strength RFI problems," *2013 IEEE International Symposium on Electromagnetic Compatibility*, Denver, CO, 2013, pp. 134-137.

[8]   Q. Huang, F. Zhang, T. Enomoto, J. Maeshima, K. Araki and C. Hwang, "Physics-Based Dipole Moment Source Reconstruction for RFI on a Practical Cellphone," in IEEE Transactions on Electromagnetic Compatibility, vol. 59, no. 6, pp. 1693-1700, Dec. 2017.

[9]   G. Li et al., "A Resonant E-Field Probe for RFI Measurements," in *IEEE Transactions on Electromagnetic Compatibility*, vol. 56, no. 6, pp. 1719-1722, Dec. 2014.

[10]   H. H. Chuang et al., "A Magnetic-Field Resonant Probe With Enhanced Sensitivity for RF Interference Applications," in *IEEE Transactions on Electromagnetic Compatibility*, vol. 55, no. 6, pp. 991-998, Dec. 2013.

[11]   S. Shinde, S. Marathe, G. Li, R. Zoughi and D. Pommerenke, "A Frequency Tunable High Sensitivity H-Field Probe Using Varactor Diodes and Parasitic Inductance," in *IEEE Transactions on Electromagnetic Compatibility*, vol. 58, no. 1, pp. 331-334, Feb. 2016

[12] H. Funato and T. Suga, "Magnetic near-field probe for GHz band and spatial resolution improvement technique," *2006 17th International Zurich Symposium on Electromagnetic Compatibility*, Singapore, 2006, pp. 284-287.

[13] N. Ando et al., "Miniaturized thin-film magnetic field probe with high spatial resolution for LSI chip measurement," *2004 International Symposium on Electromagnetic Compatibility* (IEEE Cat. No.04CH37559), 2004, pp. 357-362 vol.2.

[14] N. N. Mai-Khanh, T. Iizuka, A. Sasaki, M. Yamada, O. Morita and K. Asada, "A Near-Field Magnetic Sensing System With High-Spatial Resolution and Application for Security of Cryptographic LSIs," in IEEE Transactions on Instrumentation and Measurement, vol. 64, no. 4, pp. 840-848, April 2015.

[15] S. Jarrix, T. Dubois, R. Adam, P. Nouvel, B. Azais and D. Gasquet, "Probe Characterization for Electromagnetic Near-Field Studies," in IEEE Transactions on Instrumentation and Measurement, vol. 59, no. 2, pp. 292-300, Feb. 2010.

[16] Y. T. Chou and H. C. Lu, "Space Difference Magnetic Near-Field Probe With Spatial Resolution Improvement," in *IEEE Transactions on Microwave Theory and Techniques*, vol. 61, no. 12, pp. 4233-4244, Dec. 2013.

[17] C. F. M. Carobbi and L. M. Millanta, "Analysis of the common-mode rejection in the measurement and generation of magnetic fields using loop probes," in *IEEE Transactions on Instrumentation and Measurement*, vol. 53, no. 2, pp. 514-523, April 2004.

[18] Y. T. Chou and H. C. Lu, "Magnetic Near-Field Probes With High-Pass and Notch Filters for Electric Field Suppression," in *IEEE Transactions on Microwave Theory and Technique*s, vol. 61, no. 6, pp. 2460-2470, June 2013.

[19] Z. Yan, J. Wang, W. Zhang, Y. Wang and J. Fan, "A Simple Miniature Ultrawideband Magnetic Field Probe Design for Magnetic Near-Field Measurements," in *IEEE Transactions on Antennas and Propagation*, vol. 64, no. 12, pp. 5459-5465, Dec. 2016.

III. A PASSIVE INTERMODULATION SOURCE IDENTIFICATION MEASUREMENT SYSTEM USING VIBRATION MODULATION METHOD

ABSTRACT

A measurement system which uses acoustic vibration to locate passive intermodulation (PIM) sources in base station antennas is presented. This measurement system uses mechanical vibration to modulate the PIM signal. The modulation of the PIM signal is detected, and its strength or presence/absence is used as guidance for selecting the location of the vibrating transducer. For the method to be successful, the PIM signal must be caused by loose mechanical contacts or loose nonlinear materials. By introducing the acoustic vibration at different locations in the base station antenna and observing if the PIM signal is modulated by the acoustic frequency, the most likely location of the PIM source is identified.

1. INTRODUCTION

Passive intermodulation (PIM) is the intermodulation caused by slight nonlinearities in passive components. These slight nonlinearities create intermodulation products when these passive components are subjected to two or more high power frequency signals simultaneously. The mechanism of PIM generation has been studied in previous literature [1]-[3]. The PIM phenomenon is usually caused by either nonideal metal to metal contact or nonlinear objects (e.g., ferrous materials [4]) in or close to the RF path. In the modern wireless system, the transmitting (Tx) and receiving (Rx) paths

often share the same antenna at the same time Usually, there are multiple frequency signals in the TX path of the communication system. When the antenna creates PIM, the intermodulation products may fall into the receiving frequency band. If the antenna is also used for receiving, the created PIM signal will couple to the Rx channel and, thus, cause system sensitivity deterioration. Modern base station antennas do not only consist of antenna elements, but also other components for beam tilting purpose, such as power dividers, phase shifters, etc. The growing complexity of modern antennas makes it more likely to cause PIM problems. Thus, passing a PIM level of e.g., -153 dBc is a requirement before deploying the antennas on site [5]. The need for identifying PIM sources on base station antennas and other communication equipment is necessary.

Several approaches have been made by the academic and industrial world. In the next section, the characteristics and drawbacks of these methods are briefly discussed.

In this paper, a PIM identification measurement system is presented, the measurement system is based on the concept of vibration modulation. The challenges and concerns of building the system are also going to be discussed in later sections.

2. OVERVIEW OF PIM SOURCE IDENTIFICATION METHODS

Several approaches for locating PIM have been reported. A traditional method is to tap/manipulate all possible locations manually. Another method is to replace components until the problem is solved, which is time-consuming and very costly.

PIM analyzers nowadays have been equipped with TDR-like techniques to locate the PIM source, such as range-to-fault by Kaelus [7] and distance-to-PIM by Anritsu [8].

One implementation of such a method fixes one Tx signal and sweeps the other Tx signal over the entire available bandwidth. The frequency of the reflected PIM signal will also sweep across a certain frequency range. The inverse Fast Fourier Transform (iFFT) is performed to the reflected PIM signal to reconstruct a time-domain pulse. By looking at the amplitude and the phase of the reconstructed pulse, the position of the PIM source can be determined. The PIM analyzers inevitably have very limited operational bandwidth due to the limited bandwidth, which is determined by the cellular technology and the duplexers inside the PIM analyzer. Furthermore, the operation frequency (1 to 2 GHz) is relatively low which results in the long wavelength. All these factors lead to poor resolution accuracy which is often in the order of meters according to the manufacturers' specifications. Thus, these techniques are more suitable to find PIM sources in the feedlines of antennas, or PIM sources outside the antenna; for example, a corroded metal roof structure.

Another approach to identifying PIM sources is the near-field scan. In EMI applications [9][11], the near-field scan is performed to locate sources of the potential EMI problem. The near-field scan has also been shown to be a powerful tool to locate the PIM source on open structures such as microstrip lines and antennas [12][13]. The most basic near-field scan simply searches for the maximal field strength of the PIM signal; advanced implementation observes the phase to detect the direction of travel of the PIM signal [12][13]. The location of the maximal PIM signal strength is mostly likely to be the PIM source. However, this method cannot locate PIM sources in enclosed components like cables, phase shifters, and cavity filters. Another problem may be

caused by the proximity of the probe to the RF carrying structures: the probe itself may

cause PIM, leading to false readings.

3. VIBRATION MODULATION METHOD

Experiments with PIM sources of loose mechanical connections have shown that

the PIM signal level was highly unstable and was subject to vibration by hand [6]. Thus,

it is possible to amplitude modulate (AM) the PIM signal at the PIM source point. By

analyzing the PIM signal's side bands one is able to locate PIM sources. Challenges

include the selection of the modulation frequency, the mechanical coupling of the

vibration via the transducer to the RF carrying structure, and proper filtering and

amplification of the modulated signal. Only the correct selection of these parameters

allows creating PIM AM modulation sidebands of detectable magnitude combined with

the ability to differentiate the AM sideband levels as a function of the location of the

transducer.

The purpose of the vibration modulation method is to locate the PIM source on

the device under test (DUT) through the acoustic vibration. Vibrating a structure will

cause AM modulation at the same frequency the vibration is set to. Here, these

frequencies are in the acoustic frequency (hundreds of Hz to hundreds of kHz). The

amplitude of the PIM signal (f_{PIM}) will be modulated by the vibration frequency (for

example, 1 kHz). This means the PIM signal has an amplitude modulation of the

vibration frequency (f_{vbr}) (Figure). If the vibration position is not at the PIM source, the

PIM signal will not have any amplitude modulation. Thus, by checking the magnitude of

the AM sidebands, the PIM source can be located.
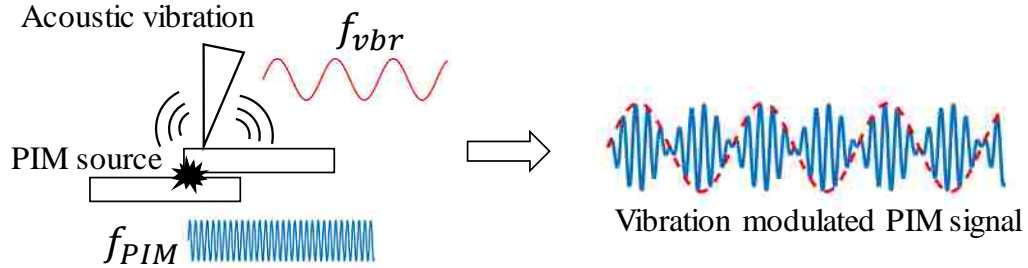
Figure 1. Vibration modulation at PIM source.

Equation (1) is a generalized model to describe the PIM generation at the PIM

source of two or more loose contact objects.

$$J = \sum_{i=0}^{\infty} g_i V^i = g_0 + g_1 V^1 + g_2 V^2 + g_3 V^3 + g_4 V^4 + \tag{1}$$

where J is the current density at the PIM source, g_i is the nonlinear conductance and V^i is

the voltage across the loose contact objects. It should be noted that the loose contact does

not necessarily cause PIM problem. The contact condition determines the PIM

performance. In this paper, only the loose contact cases that cause PIM problem are

considered.

The third order term in (1) represents the third PIM. Previous studies [14] have

shown that the value of this nonlinear conductance is associated with the distance

between the loose metal parts. The external vibration will change the distance between

the loose parts at a frequency of f_{vbr} and, thus, lead to a periodical change in the value of g_3. This is essentially amplitude modulation. The vibration modulated PIM signal can be described as

$$J_{PIM3} = K(f_{vbr})g_{30}V^3, \qquad (2)$$

where $K(f_{vbr})$ is the amplitude modulation factor caused by applying external vibration at the PIM source, and g_{30} is the nominal nonlinear conductance value when no vibration is applied.

An acoustic modulation method for PIM source identification was first reported in [6]. In [6], the authors used an acoustic horn to deliver acoustic waves to the DUT antenna through the air. The acoustic frequency used in their work was between 10 kHz and 50 kHz. The PIM signal level reported in [6] was as high as -25 dBm. The AM sideband was 30 dB to 40 dB below the carrier frequency which is the third order PIM signal. This method cannot be applied to modern base station antenna PIM tests directly for several reasons. First, the method described in [6] used UHF and HF signals to create PIM. The standard PIM tests [16] of base station antenna requires two transmitting (Tx) signals in the same band, at 43 dBm (20 W) each (Figure 2). Second, coupling through air is inefficient and does not localize well. In this proposed measurement system, the vibration is delivered to the DUT through direct contact. Third, the PIM level tested in [6] was -23 dBm, which is much higher than the requirement for base station antennas [17]. Often –110 dBm are required for passing. The sidebands of the vibration modulation will be at least 30 dB, but sometimes 60 dB below the PIM signal. These

weak signals in presence of the two 20 W carriers pose a major obstacle in the successful implementation of the vibration modulation method.
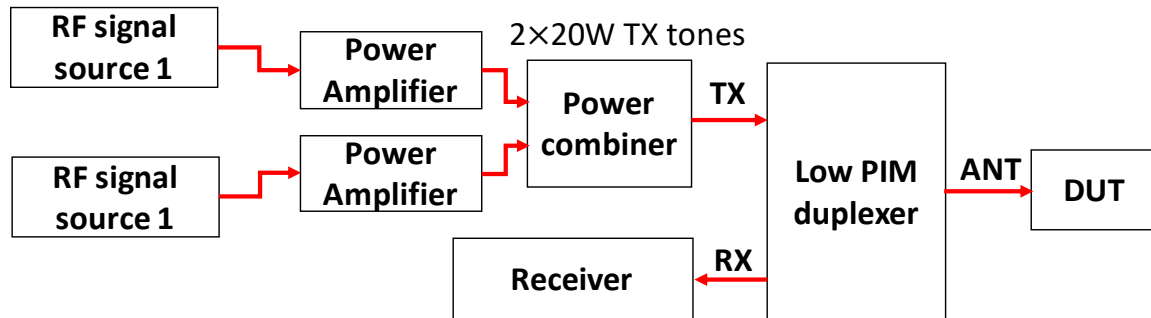
Figure 2. Reflective PIM testing [17].

3.1. ACOUSTIC VIBRATION SYSTEM

The goals of the acoustic vibration system are 1) to create sufficient vibration on the DUT, and 2) to not generate unacceptable acoustic noise during the tests.

Several acoustic sources within the frequency range from 100 Hz to 100 kHz were studied for the proposed vibration modulation method. A DC motor rotating at 100 Hz is an example. However, at 100 Hz the complete antenna will vibrate making it difficult to locate the PIM source. With rising frequency, the ability of locating the PIM source improved. However, within the range of 100 Hz to 20 kHz hazardous noise levels made it impossible to operate the system in spite of hearing protection. Acoustic transducers typically used for acoustic cleaning were selected as acoustic vibration sources. Economic high output transducers are readily available.

3.1.1. Acoustic Transducer Acoustic transducers convert electrical energy to mechanical vibration [19]. They contain a piezoelectric substrate layer between two metal

parts. While other frequencies have been tested, most of the results shown are based on the acoustic transducers (Figure 3) at about 10 W input level.
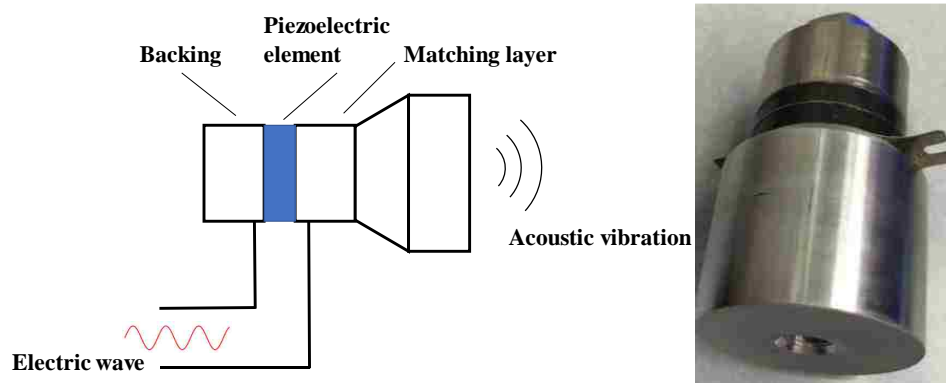
Figure 3. Illustration of acoustic transducer mechanism.

3.1.2. Acoustic Signal Generation Resolution bandwidths of down to 1 Hz are used. To avoid the need for peak-tracking, the frequency should be stable within less than 1 Hz. This requires stable, possibly frequency locked, PIM TX sources and a stable acoustic frequency. For example, if the vibration is induced by a motor at 100 Hz then its rotation speed will not be sufficiently well controlled to allow 1 Hz RBW. The vibration system needs to allow adjusting the frequency, as temperature, pressure on the transducer and other factors cause small (up to 1 kHz) variation of the resonant frequency of the transducer. A commercial signal generator is used in the system to generate a sinusoidal wave at the acoustic frequency.

The vibration system will also need to monitor output voltage and/or current, for easier tuning of the resonance frequency and for the protection of the transducer.

The block diagram of the acoustic vibration system is shown in Figure 4. The photo of the final version of the acoustic vibration system is shown in Figure 5.
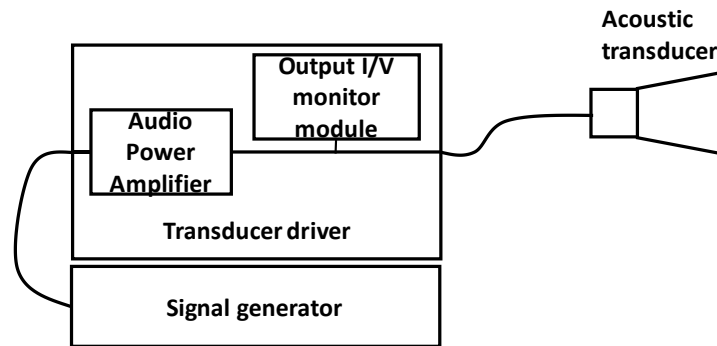
Figure 4. Block diagram of acoustic vibration system.
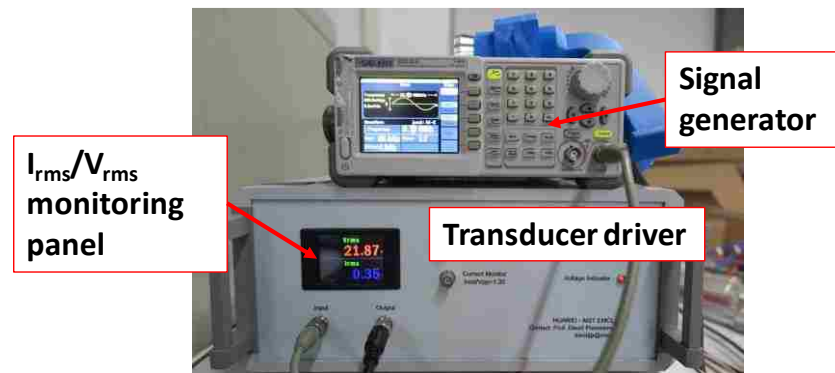
Figure 5. Photo of the acoustic vibration system, the final version.

3.1.3. Vibration Transfer Structure A vibration transfer structure allows transfer of the vibration to the testing point on the DUT. Such structures should be able to inject the vibration locally onto the DUT, and it should minimize damage to the surface of the DUT during the vibration. Maximal vibration transfer is desired for achieving the strongest amplitude modulation. The structure cannot have electrical contact with the DUT as these would cause PIM. At last, the structure itself should not cause PIM although it may be within cm of the radiating antenna elements.

A substrate rod was selected as the vibration delivery structure in the vibration system, as shown in Figure 6. The substrate rod is non-conducting. It is connected to the

acoustic transducer body with a piece of brass tube. The substrate rod was glued to the

brass tube. Then, the brass tube was screwed tightly to the transducer body. The substrate

rod structure was durable, and it did not cause damage to the DUT as its tip could be

rounded

Figure 6. Vibration delivery structure: substrate rod.

3.1.4. Vibration Strength Measurement As explained in Section III, the

amplitude modulation is correlated to the distance between the loose contact objects at the

PIM source. Furthermore, it is desirable that the vibration is restricted to a small region so

that when vibrating at other places, the PIM source will not be vibrated as well. Thus, it is

important to understand the vibration strength that can be delivered to the DUT by the

acoustic transducer as well as the vibration distribution on the DUT. An accelerometer

sensor (model 352A73 [20]) from PCB piezoeletronics with a signal conditioner (model

480C02 [21]) was selected in this work to measure the vibration displacement. The

accelerometer was used to measure the displacement of the vibration to characterize the

vibration strength on the DUT.

The accelerometer was attached to the DUT by adhesive (Figure 7). It measures

the acceleration along the z-axis. The sensor factor is 0.498 mV/m/s^2, which means that

for 1 m/s^2 acceleration the sensor's output amplitude is 0.498 mV.
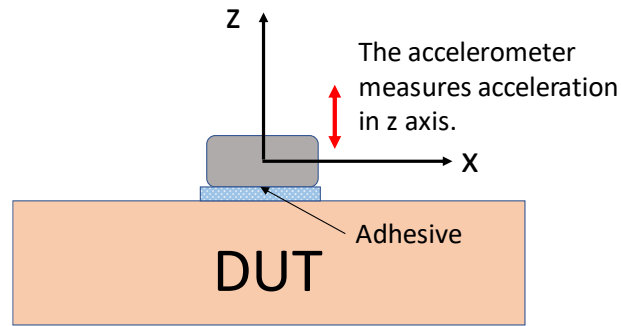
Figure 7. The accelerometer is attached to the DUT by adhesive.

For sinusoidal vibration, within a single period, the displacement and acceleration have the following relation:

$$d = \iint a(\omega t) dt^2, \tag{3}$$

where d is the displacement in the time domain, and a is the acceleration in the time domain. For time-harmonic signal, its relation in the frequency domain is:

$$D(\omega) = \frac{A(\omega)}{\omega^2}, \tag{4}$$

where $D(\omega)$ is the displacement at ω, and $A(\omega)$ is the acceleration.

The vibration strength measurement set-up is shown in Figure 8. The DUT is a phase shifter on the backside of a base station antenna which will be explained in detail in Section IV. The accelerometer was attached to the lid of the phase shifter by super glue. The transducer was set to about 10 W input power. The sensor output waveform was

processed with Fast Fourier Transform (FFT) in the oscilloscope so that the signal

amplitude at acoustic transducer's operating frequency can be identified.
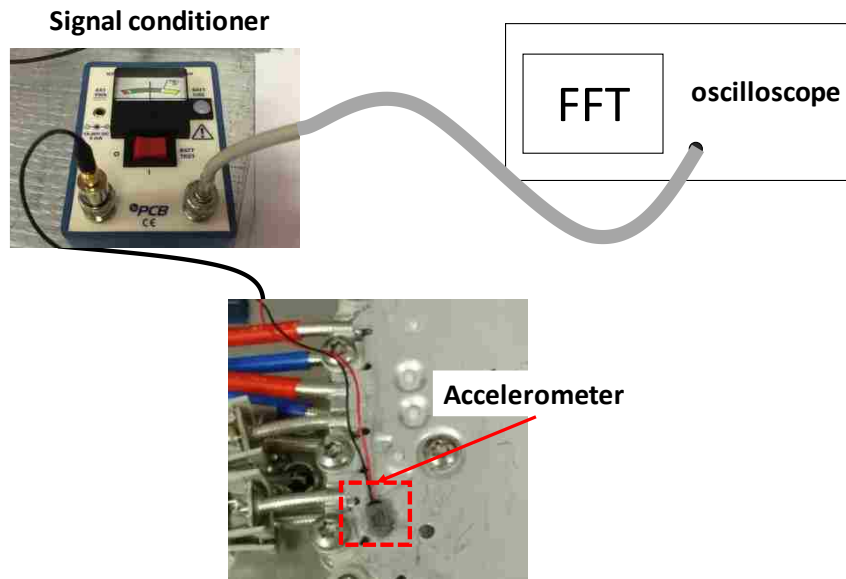
Figure 8. Vibration strength measurement using the accelerometer.
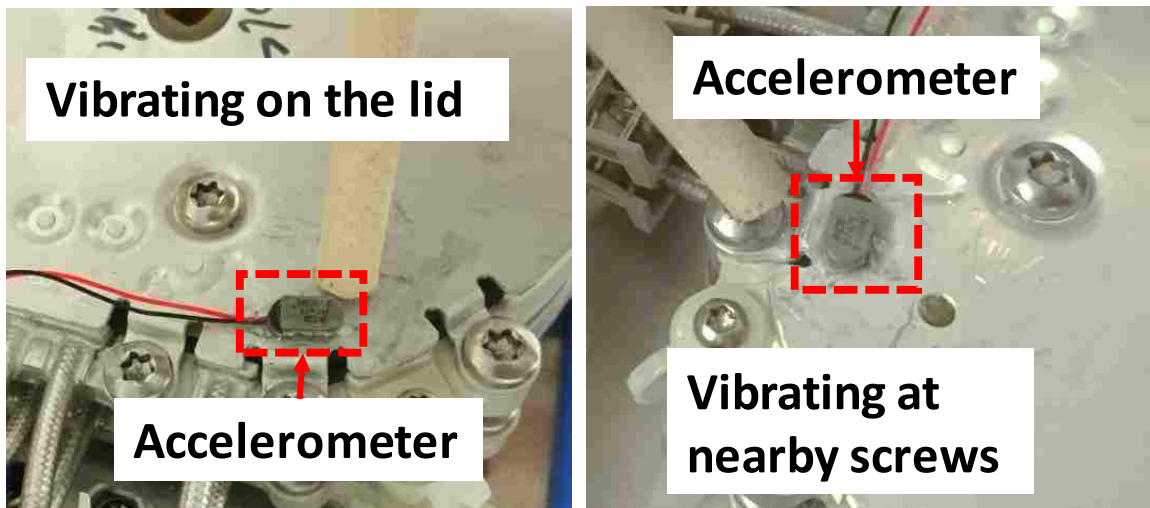
Figure 9. Left: vibrating on the lid. Right: vibrating at nearby screws.

Two types of locations were tested: the lid and the screws nearby (Figure 9). For vibrating on the lid, the maximum magnitude at the transducer's operating frequency was 0 dBV, while vibrating at the nearby screws the maximum magnitude was -17 dBV. Using (4), the calculated displacement values are 88.55 nm for vibrating on the lid and 12.5 nm for vibrating at nearby screws.

It is worth noting that the acoustic vibration was significantly attenuated (17 dB) while propagating from screws to the lid. It is a desirable characteristic that the vibration is only limited to the screw that is being vibrated. The vibration at other screws will not cause modulated sideband at the PIM source screws.

3.2. DEMODULATION SYSTEM FOR DETECTING VIBRATION MODULATED PIM SIGNALS

A demodulation system is needed to identify the AM modulation. A spectrum analyzer (SA) can be used in two ways: observe on side band at very narrow RBW setting (e.g., 10 Hz), or demodulate the AM in zero span mode using a resolution bandwidth that is at least twice as wide as the modulation frequency to capture the carrier and both side bands. The oscilloscope is an alternative to observe side bands. It offers the advantage of synchronous detection as the vibrating frequency can be used for triggering and averaging to improve the signal to noise ratio (SNR), but it will increase the measurement time. The oscilloscope is triggered on the external vibration frequency signal and then averaging is performed on the time domain waveforms before performing FFT. This will reduce the noise floor further According to authors experience, the SNR could be improved by 3-6 dB compared to the SA, when demodulating the same signal. Thus, the oscilloscope is a better instrument for detecting extremely weakly modulated

signals in this work. In the practical implementation one needs to consider the cross-coupling between oscilloscope channels. If a strong replica of the vibration drive signal is input to one channel, the cross-coupling will lead to false signals in the main channel. The replica of the vibration drive signal may need to be attenuated to mV levels to avoid this problem.

Proper filtering and amplifying of the vibration modulated PIM signal is needed before performing demodulation with the SA/oscilloscope. The block diagram of the demodulation system is shown in Figure 10. An LNA block is placed at the input of the system. The LNA stage has 2 dB Noise Figure (NF). The spectrum of the input signal not only contains the PIM signal and its side bands, but also contains two transmitting tones. These are attenuated by the duplexer, however, they may be strong enough to cause intermodulation in the demodulation system. The gain of the first amplifier stage needs to be as low as possible, but still large enough to obtain the required system noise figure; the LNA needs a high third order Intercept Point (IP3). The LNA used in the demodulation has the output IP3 of 35.6 dBm at 2 GHz. A surface acoustic wave (SAW) filter in the cellular band is added after the LNA to suppress the Tx signals. To avoid reducing the noise figure by the SAW filter loss, one has to place these filters after the LNA. The bandwidth of the SAW filter (120 kHz) was selected to cover the slide bands of the AM modulation signal. The SAW filter works at another frequency, this requires to down-mix the input signal to this IF frequency.

An envelope detector is required before the signal can be analyzed by an oscilloscope. A log-detector IC was selected for its broad operating frequency and high dynamic range. The dynamic range of the log detector reaches from -65 dBm to 10 dBm.

The demodulation system was tested with -110 dBm RF signal with -50 dBc AM sidebands. The sideband was detected instantly.

4. MEASUREMENT VERIFICATION

4.1. MODIFICATION OF THE PIM ANALYZER

Two 20 W RF signals are needed in the PIM testing. However, the intermodulation level of these signals must be <-160 dBc and the phase noise must be low enough to measure AM sidebands (-50 dBc).

The PIM analyzer used in this work is CCI PIMPro1921 [22]. This analyzer works on bands PCS 1900 and AWS 2100. Receive frequencies are 1850-1910 MHz/1710-1755 MHz, transmit frequencies are 1930-1990 MHz/2110-2155 MHz. The adjustable output power range is 17 to 46 dBm $\times$ 2 tones.

The PIM analyzer was modified for the proposed measurement system and allowed us to measure the modulated PIM signal by the demodulation system. The modified PIM analyzer block diagram is shown in Figure 11.

4.2. ANTENNA UNDER TEST

The base station antenna used in this set-up had a typical PIM level of -120 dBm across the working frequency. The standard for PIM requires a pass level of -97 dBm/-140 dBc (2×43 dBm Tx tones) [16][17]. PIM sources can be artificially introduced into the antenna. The artificial PIM sources can be bad soldering on a location that connects two coax cables, loose screws on the phase shifter, loose antenna elements, loose metal parts, and metallic debris or ferrite on the power dividers.
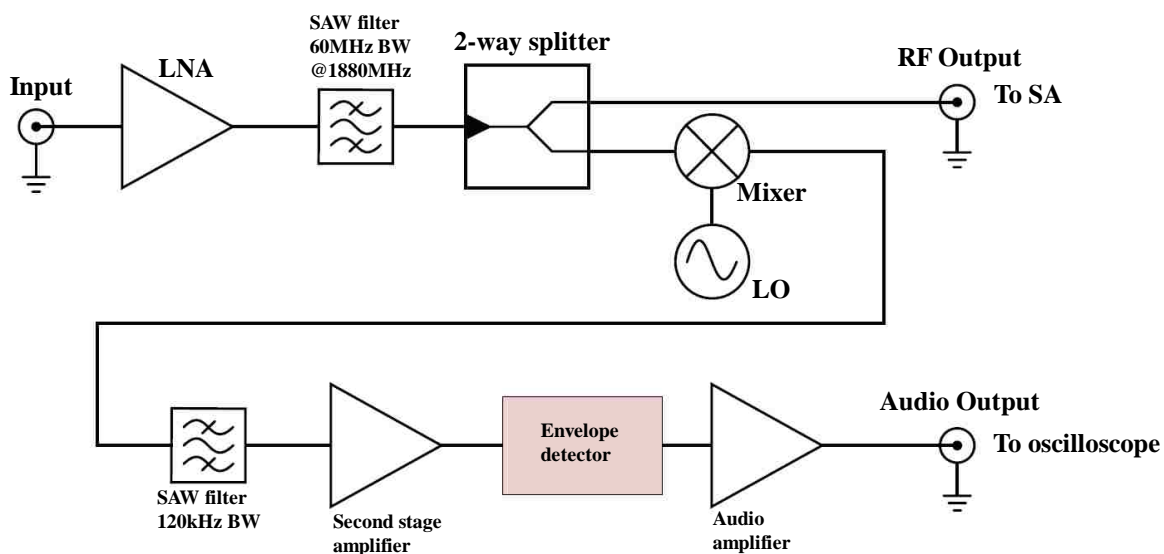
Figure 10. Block diagram of the demodulation system.

4.3. MEASUREMENT SET-UP

The vibration modulation measurement set-up diagram is shown in Figure 12 and

a photo of the set-up is shown in Figure 13. The measurements were performed in the

low PIM 3-meter semi-anechoic chamber to avoid PIM by surrounding metal parts.

For the measurement, the PIM analyzer Tx port was connected to the base station antenna

via a low-PIM cable. The PIM analyzer, low-PIM cable, and antenna use 7/16 type low-

PIM connectors. The two TX signals were set to 43 dBm. The PIM level was first

measured at the SA in order to determine the system PIM level without the intended PIM

source.

4.4. MEASUREMENT RESULTS

Two types of PIM sources were created on the components on the back side of the

antenna: Nickel-Zinc ferrite pieces on the power divider and loose phase shifter screws.

4.4.1. Ferrite Debris as PIM Source The PIM level before adding the ferrite was <-110 dBm; adding the ferrite increased the PIM level to about -100 dBm. The vibration was then applied to two locations, the PIM source and a nearby point approximately 1 cm away, and the modulated sideband was detected only at the PIM source location (Figure 15).
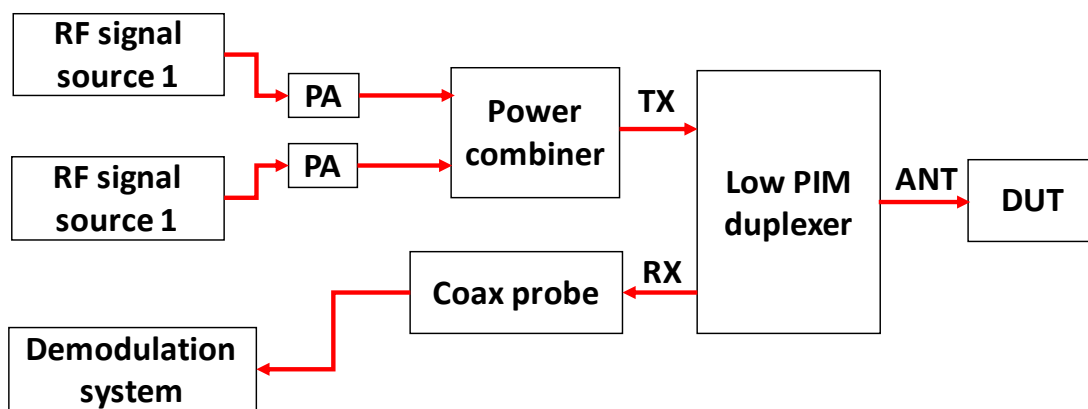
Figure 11. Block diagram of the modified PIM analyzer.
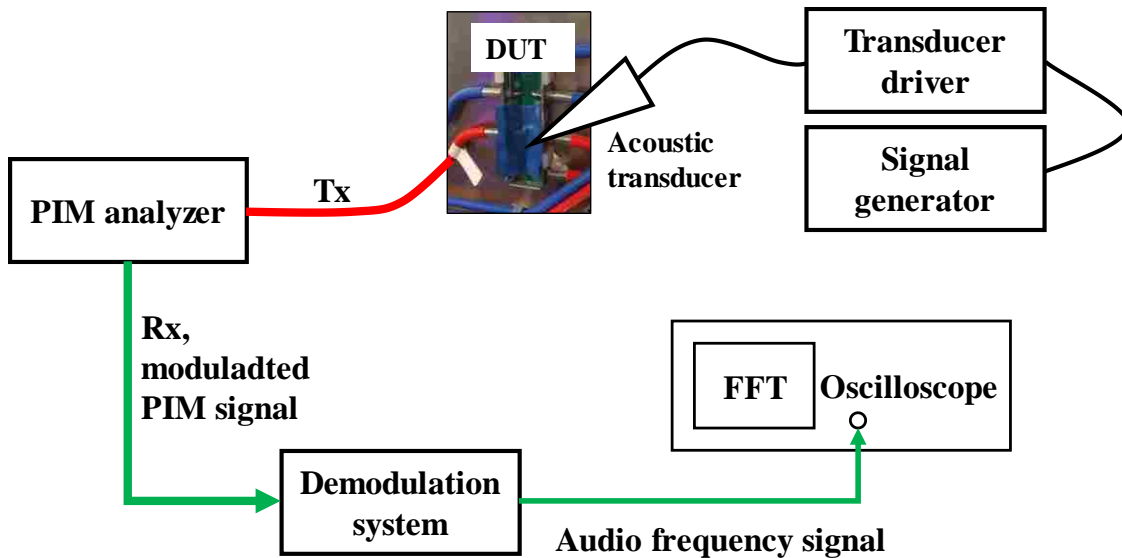
Figure 12. Block diagram of vibration modulation test system set-up.
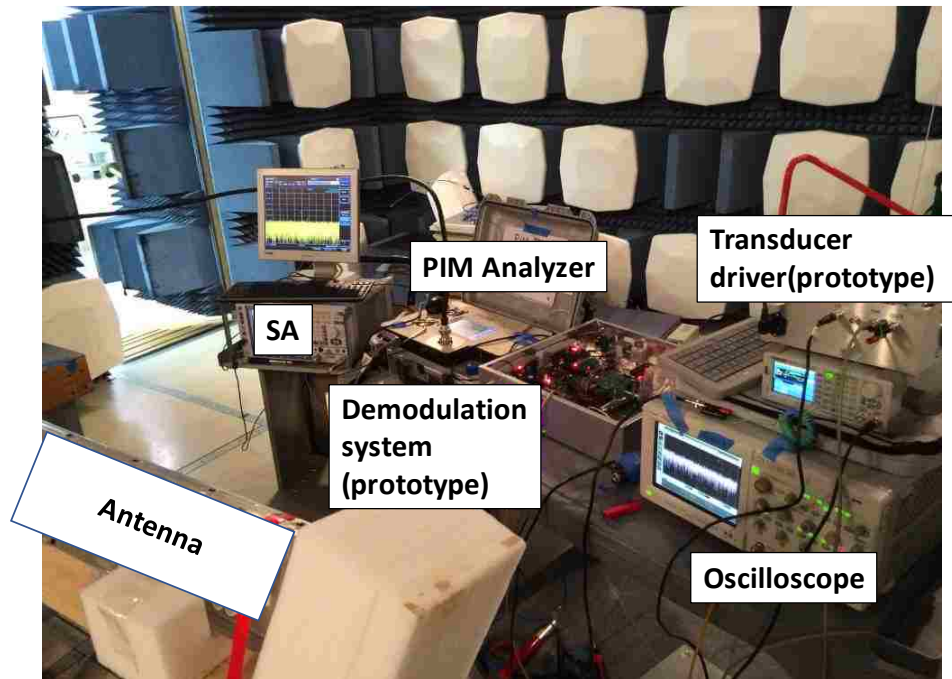
Figure 13. Photo of the set-up of the vibration modulation test system.
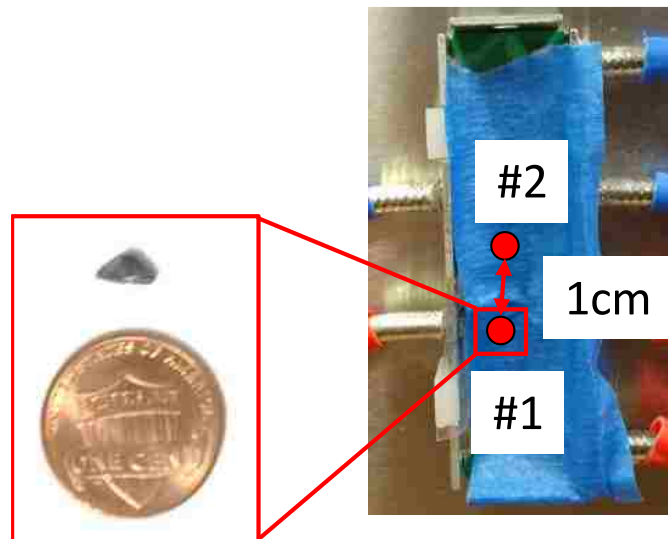
Figure 14. Ferrite debris as PIM source on power divider.

The measurement results are shown in Table 1. For ferrite debris as the PIM source case, the modulated signal was detected while vibrating at the PIM source point.

The modulated signal's SNR was 11 dB. When vibrated at the nearby point 1 cm away

from the PIM source point, the modulated signal was not detectable.
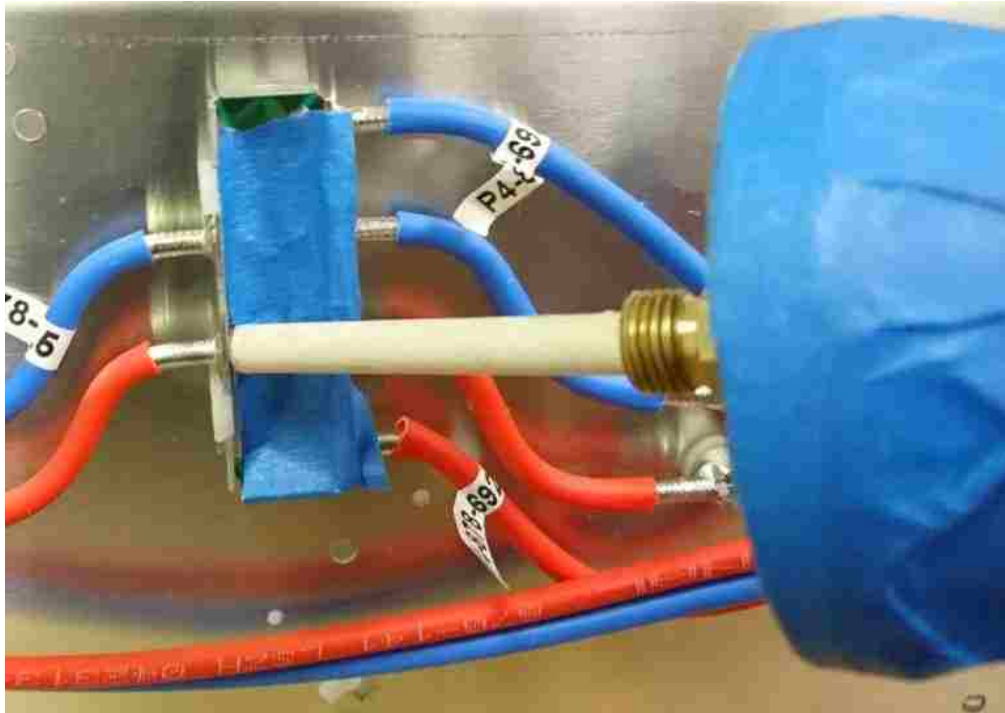
Figure 15. Performing acoustic vibration at the power divider with ferrite debris as PIM
source.

Table 1. Measurement results for ferrite debris case.

Location	Modulated sideband signal strength
#1 (PIM source)	Detected, 11 dB SNR
#2 (1 cm away)	Not detectable

A more likely PIM source on a base station antenna would be loose contact

between metal parts (for example, loose screws or loose connectors). The next

experiment tested the loose screws as the PIM source.

4.4.2. Loose Screw as PIM Source The phase shifter (Figure 16) is a component which is mounted on the backside of the antenna. It is reported that the loose screws on the phase shifter are very likely to cause PIM problems. Thus, in this measurement, one screw near the coax cable was intentionally loosened to induce a PIM problem. The test was made while the PIM level was about -100 dBm. As shown in Table 2, the sideband was detected at the PIM source screw; while vibrating at other screws the sideband signal was not detectable. As mentioned in the vibration strength measurement in Section III, the acoustic vibration attenuated as much as 17 dB while propagating from the screw to the lid. Thus, the vibration would be attenuated further from one screw to another screw. The proposed measurement system has successfully pinpointed the PIM source in the loose screw case.
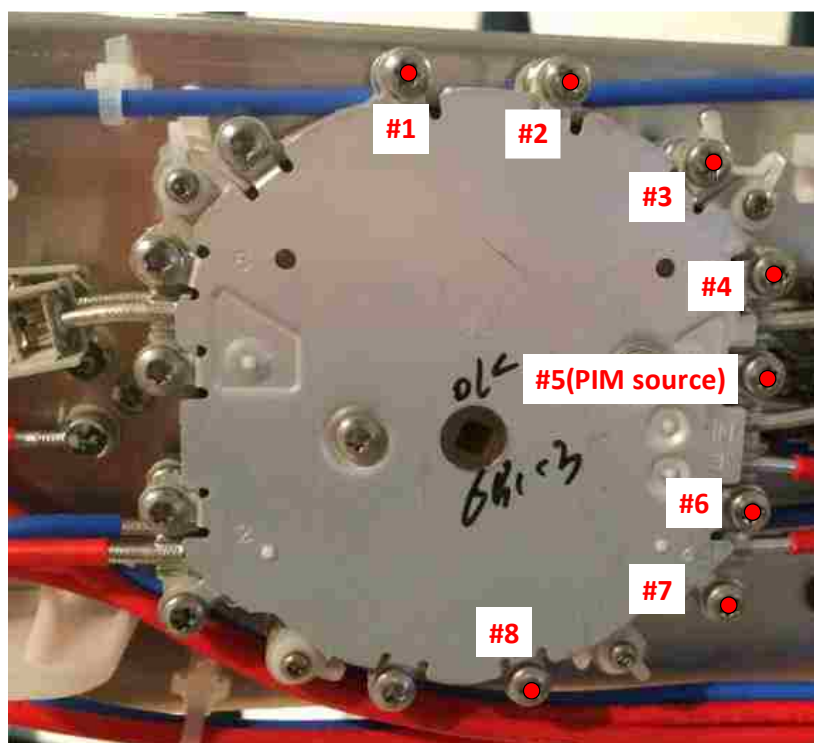
Figure 16. Eight screws (marked by red dots) were tested.

5. CONCLUSION

A PIM source identification measurement system using vibration modulation is presented. The PIM source identification system consists of two subsystems, the demodulation system and the acoustic vibration system. The demodulation system was used to detect the sideband of the vibration-modulated PIM signal from a PIM analyzer. The acoustic vibration system provided a vibration source for the system. In this work, the vibration modulation measurement system was tested on a base station antenna. The results showed that the proposed method could locate the PIM source accurately.

The measurement system was deployed on the production line to identify the PIM sources on various types of the antenna products. The proposed measurement system has identified PIM sources on all the antennas tested. On the other hand, the proposed measurement system was tested with other products other than the base station antennas, such as duplexers. However, the duplexers are made from solid metal blocks. The acoustic wave could propagate through the entire structure and form standing wave. It is impossible only to vibrate one region of the structure. Thus, the method can determine that the duplexer is causing PIM. However, it cannot locate the loose contact PIM source within the duplexer. In this worst-case scenario, the proposed measurement system can locate the PIM sources to the component level. Even when this drawback is taken into consideration, the proposed method is still more accurate in locating PIM sources than the current existing TDR-like methods mentioned in Section II, whose accuracy is in the order of meters. Overall, this system adds one tool to the tool-set of the engineers involved in design and production of low PIM devices.

Table 2. Measurement results for loose screw case.

Screw #	Modulated sideband signal strength
1	Not detectable
2	Not detectable
3	Not detectable
4	Not detectable
5(PIM source)	Detected, 10 dB SNR
6	Not detectable
7	Not detectable
8	Not detectable

REFERENCES

[1]　F. Arazm and F. A. Benson, "Nonlinearities in metal contacts at microwave frequencies," IEEE Trans. Electromagn. Compat., vol. 22, pp. 142–149, Aug. 1980.

[2]　P. L. Lui and A. D. Rawlins, "Passive nonlinearities in antenna systems," in Proc. IEE Colloquium Passive Intermodulation Products Antennas and Related Structures Tech. Dig., London, U.K., June 1989, pp. 6/1–6/7.

[3]　J. S. Petit and A. D. Rawlins, "The impact of passive intermodulation on specifying and characterizing components," in Proc. 3rd ESA Electronic. Components Conf., Noordwijk, The Netherlands, Apr. 1997, pp. 45–49.

[4]　X. Chen and Y. He, "Reconfigurable Passive Intermodulation Behavior on Nickel-Coated Cell Array," in IEEE Transactions on Electromagnetic Compatibility, vol. 59, no. 4, pp. 1027-1034, Aug. 2017.

[5]   Microwave journal,"Passive Intermodulation (PIM) Testing Moves to the Base Station", [Online]. Available: http://www.microwavejournal.com/articles/11103-passive-intermodulation-pim-testing-moves-to-the-base-station

[6]   J. C. Mantovani and H. W. Denny, "Technique for Locating Passive Intermodulation Interference Sources," 1984 National Symposium on Electromagnetic Compatibility, San Antonio, Texas, USA, 1984, pp. 1-5.

[7]   Anritsu, Understanding PIM, 2014. [Online]. Available: http://www.anritsu.com/en-US/Products-Solutions/Solution/Understanding-PIM.aspx

[8]   Kaelus, Range to Fault Technology White Paper, 2013. [Online]. Available: http://www.kaelus.com/getmedia/d408022c-d885-4880-adef-1d2e223772c3/Range-to-Fault-Tech.pdf.aspx?ext=.pdf

[9]   Anritsu, Using Distance-to-PIM (DTP) and Distance-to-Fault (DTF) trace overlay to speed site repair, 2013. [Online]. Available: https://dl.cdn-anritsu.com/en-us/test-measurement/files/Application-Notes/Application-Note/11410-00869A.pdf

[10]   T. Li, V. Khilkevich and D. Pommerenke, "Phase-Resolved Near-Field Scan Over Random Fields," in IEEE Transactions on Electromagnetic Compatibility, vol. 58, no. 2, pp. 506-511, April 2016.

[11]   G. Li, K. Itou, Y. Katou, N. Mukai, D. Pommerenke and J. Fan, "A Resonant E-Field Probe for RFI Measurements," in IEEE Transactions on Electromagnetic Compatibility, vol. 56, no. 6, pp. 1719-1722, Dec. 2014.

[12]   S. Hienonen, V. Golikov, P. Vainikainen and A. V. Raisanen, "Near-field scanner for the detection of passive intermodulation sources in base station antennas," in IEEE Transactions on Electromagnetic Compatibility, vol. 46, no. 4, pp. 661-667, Nov. 2004.

[13]   A. Shitvov, A. Schuchinsky and D. Zelenchuk, "Near-field mapping of passive intermodulation in printed circuits," Proceedings of the Fourth European Conference on Antennas and Propagation, Barcelona, Spain, 2010, pp. 1-4.

[14]   X. Zhao et al., "Analytic passive intermodulation model for flange connection based on metallic contact nonlinearity approximation," in IEEE Transactions on Microwave Theory and Techniques , vol.PP, no.99, pp.1-9, 2017 .

[15]   C. Vicente and H. L. Hartnagel, "Passive-Intermodulation Analysis Between Rough Rectangular Waveguide Flanges," in IEEE Transactions on Microwave Theory and Techniques, vol. 53, no. 8, pp. 2515-2525, Aug. 2005.

[16] International Electrotechnical Commission "International Standard: RF connectors, connector cable assemblies and cables - intermodulation level measurement", IEC 62037.

[17] Anritsu, Passive Intermodulation (PIM), 2013 [Online]. Available: https://www.anritsu.com/en-US/test-measurement/technologies/pim

[18] Maxim Integrated, Three Methods of Noise Figure Measurement, 2014 [Online]. Available: https://www.maximintegrated.com/en/app-notes/index.mvp/id/2875

[19] K. Uchino, "Introduction to piezoelectric actuators and transducers," International Conference on Intelligent Materials (5th), Smart Systems & Nanotechnology (2003), pp. 1–40.

[20] PCB Piezotronics, Accelerometer Model 352A73 datasheet, 2013. [Online]. Available: https://www.pcb.com/products.aspx?m=352A73

[21] PCB Piezotronics, Signal conditioner Model 480C02 datasheet, 2013. [Online]. Available: http://www.pcb.com/Products.aspx?m=480C02

[22] CCI PIMPro1921 datasheet, 2008. [Online]. Available: http://www.cciproducts.com/www2/index.php/products/pim-analyzers/pimpro-analyzers/item/291

SECTION

2. CONCLUSIONS

Spring contacts are used in mobile devices to ground the metal planes near the antennas. Inappropriate design of the spring contact will cause harmonic generation at the contact which will deteriorate the receiver sensitivity of the mobile system.

In the first paper, the RF passive harmonic generation phenomenon on the spring contact is studied. A spring contact harmonic generation measurement system is developed. The factors that may have an impact on the spring contact harmonic generation, such as contact material, contact force, and contact resistance are characterized by the measurement system. The gold-to-gold contact is found to be much superior to the stainless-steel contacts. It is also found that the passive nonlinearity at the spring contact is the semiconductor-like junction formed by the surface oxide film.

In the second paper, we show that the maximum E-field coupling occurs at a location slightly offset from the trace center. The E-field coupling to a shielded H-field probe at such a position leads to differential mode coupling which the standard shield of an H-field probe is unable to suppress. The coupling mechanism is investigated and a differential E-field coupling suppression approach is proposed. For the H-field probe used in this work, a proposed floating plate is shown to improve the measured E-field suppression ratio by a factor of 18 dB compared to a similar probe without this modification.

In the third paper, a measurement system which uses acoustic vibration to locate passive intermodulation (PIM) sources in base station antennas is presented. This measurement system uses mechanical vibration to modulate the PIM signal. The modulation of the PIM signal is detected, and its strength or presence/absence is used as guidance for selecting the location of the vibrating transducer. For the method to be successful, the PIM signal must be caused by loose mechanical contacts or loose nonlinear materials. By introducing the acoustic vibration at different locations in the base station antenna and observing if the PIM signal is modulated by the acoustic frequency, the most likely location of the PIM source is identified.

BIBLIOGRAPHY

[1]   Sen Yang, Qiaolei Huang, Guanghua Li, Reza Zoughi and David J. Pommerenke, "Differential E-Field Coupling to Shielded H-Field Probe in Near-Field Measurements and a Suppression Approach," in IEEE Transactions on Instrumentation and Measurement, vol. 67, no. 12, pp. 2872-2880, Dec. 2018.

[2]   G. Shen, S. Yang, J. Sun, S. Xu, D. J. Pommerenke and V. Khilkevich, "Maximum Radiated Emissions Evaluation for the Heatsink/IC Structure Using the Measured Near Electrical Field," in *IEEE Transactions on Electromagnetic Compatibility*, vol. 59, no. 5, pp. 1408-1414, Oct. 2017.

[3]   S. Yang, P. Maheshwari, V. Khilkevich and D. J. Pommerenke, "Coupling path visualization using a movable scatterer," 2014 IEEE International Symposium on Electromagnetic Compatibility (EMC), Raleigh, NC, 2014, pp. 707-711.

[4]   S. Yang and D. J. Pommerenke, "Effect of Different Load Impedances on ESD Generators and ESD Generator SPICE Models," in IEEE Transactions on Electromagnetic Compatibility, vol. PP, no. 99, pp. 1-8.

[5]   S. Yang, A. Bhandare, H. Rezaei, W. Huang and D. J. Pommerenke, "Step-Response-Based Calibration Method for ESD Generators in the Air-Discharge Mode," in IEEE Transactions on Electromagnetic Compatibility, vol. PP, no. 99, pp. 1-4.

[6]   J. Zhou et al., "An ESD demonstrator system for evaluating the ESD risks of wearable devices," 2017 39th Electrical Overstress/Electrostatic Discharge Symposium (EOS/ESD), Tucson, AZ, 2017, pp. 1-7.

[7]   G. Shen, S. Yang, V. Khilkevich, D. Pommerenke, H. Aichele, D. Eichel, C. Keller, "Simple D flip-flop behavioral model of ESD immunity for use in the ISO 10605 standard," 2014 IEEE International Symposium on Electromagnetic Compatibility (EMC), Raleigh, NC, 2014, pp. 455-459.

[8]   Oganezova, G. Shen, S. Yang, D. Pommerenke, V. Khilkevich and R. Jobava, "Simulation of ESD coupling into cables based on ISO 10605 standard using method of moments," 2016 IEEE International Symposium on Electromagnetic Compatibility (EMC), Ottawa, ON, 2016, pp. 701-706.

[9]   S. Yang, J. Zhou, D. Liu, D. Pommerenke, "A Simple Frequency Response Compensation Method for Current Probe Measurements of ESD Currents," 2017 International Symposium on Electromagnetic Compatibility (EMC), Washington DC, 2017, pp. 158-163.

[10]   G. Shen, S. Yang, V. Khilkevich, D. Pommerenke, H. Aichele, D. Eichel, C. Keller, "ESD Immunity Prediction of D Flip-Flop in the ISO 10605 Standard Using a Behavioral Modeling Methodology," in *IEEE Transactions on Electromagnetic Compatibility*, vol. 57, no. 4, pp. 651-659, Aug. 2015.

[11]   Sen Yang, Xiong Chen, Javad Meiguni, Jeff Qi, Cheung-Wei Lam, and David Pommerenke, "Experimental characterization of the harmonic generation at the spring contact in a mobile device," to be submitted to IEEE Transactions on Electromagnetic Compatibility

[12]   Sen Yang, Xiong Chen, Javad Meiguni, Jeff Qi, Cheung-Wei Lam, and David Pommerenke, "Worst-case estimation of the spring contact harmonic generation at the antenna in a mobile device," to be submitted to IEEE Transactions on Electromagnetic Compatibility

[13]   S. Yang, W. Wu, S. Xu, Y. J. Zhang, D. Stutts and D. J. Pommerenke, "A Passive Intermodulation Source Identification Measurement System Using a Vibration Modulation Method," in *IEEE Transactions on Electromagnetic Compatibility*, vol. 59, no. 6, pp. 1677-1684, Dec. 2017.

[14]   Shaohui Yong, Sen Yang, Ling Zhang, Xiong Chen, David Pommerenke, Victor Khilkevich, "Passive Intermodulation Source Localization Based on Emission Source Microscopy,", to appear in in IEEE Transactions on Electromagnetic Compatibility

[15]   Xiong Chen, Yongning He, Sen Yang, Anfeng Huang, Yaojiang Zhang, David J Pommerenke, Jun Fan, "Coplanar Intermodulation Reference Generator Using Substrate Integrated Waveguide With Integrated Artificial Nonlinear Dipole," in IEEE Transactions on Electromagnetic Compatibility.

[16]   Xiong Chen, Yongning He, Sen Yang, Wanzhao Cui, Yao-Jiang Zhang, David J Pommerenke, Jun Fan, "Analytic Passive Intermodulation Behavior on the Coaxial Connector Using Monte Carlo Approximation," in IEEE Transactions on Electromagnetic Compatibility, vol. 60, no. 5, pp. 1207-1214, Oct. 2018.

[17]   S. Shinde, S. Yang, N. Erickson, D. Pommerenke, C. Ding, D. White, S. Scearce, Y. Yang, "Electro-mechanical structures for channel emulation," 2014 IEEE International Symposium on Electromagnetic Compatibility (EMC), Raleigh, NC, 2014, pp. 939-944.

VITA

Sen Yang was born in Hebei Province, P.R. China. He received his Bachelor of Science degree in Electromagnetics and Radio Technology (2012) from University of Science and Technology of China (UESTC) and Master of Science in Electrical Engineering (2016) from Missouri University of Science and Technology. He started his Ph.D. program in 2016 in the Electrical and Computer Engineering Department in Missouri University of Science and Technology. He received his Ph.D. degree in Electrical Engineering in July 2019 from Missouri University of Science and Technology.